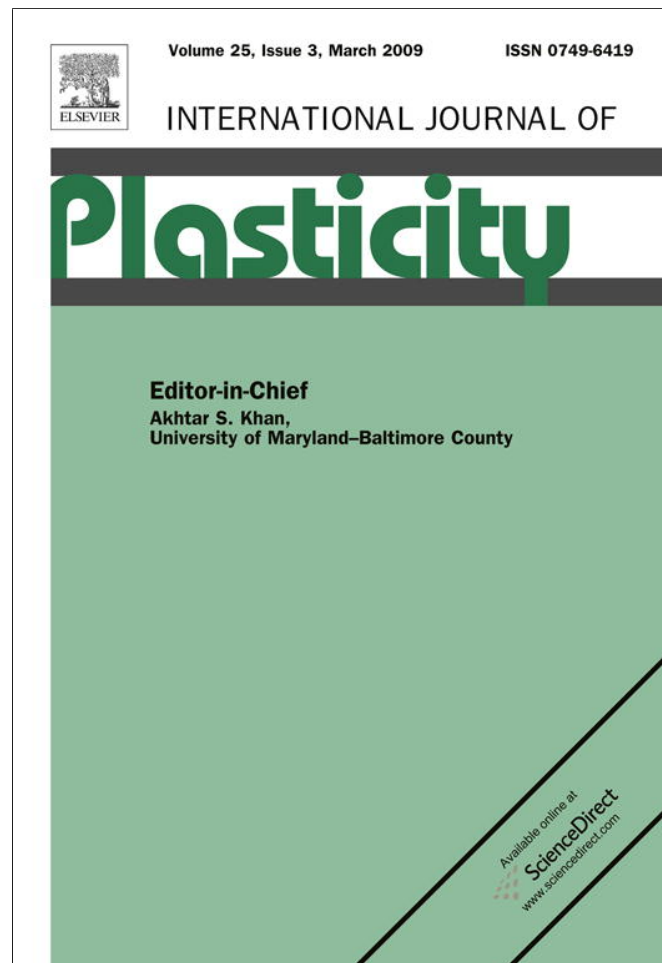


Provided for non-commercial research and education use.
Not for reproduction, distribution or commercial use.



This article appeared in a journal published by Elsevier. The attached copy is furnished to the author for internal non-commercial research and education use, including for instruction at the authors institution and sharing with colleagues.

Other uses, including reproduction and distribution, or selling or licensing copies, or posting to personal, institutional or third party websites are prohibited.

In most cases authors are permitted to post their version of the article (e.g. in Word or Tex form) to their personal website or institutional repository. Authors requiring further information regarding Elsevier's archiving and manuscript policies are encouraged to visit:

<http://www.elsevier.com/copyright>



Micromechanical modeling of stress-induced phase transformations. Part 2. Computational algorithms and examples

Valery I. Levitas^{a,b,*}, Istemi B. Ozsoy^{b,c}

^a *Iowa State University, Departments of Mechanical Engineering, Aerospace Engineering and Material Science and Engineering, Ames, Iowa 50011, USA*

^b *Texas Tech University, Department of Mechanical Engineering, Lubbock, TX 79409, USA*

^c *TOBB University of Economics and Technology, Department of Mechanical Engineering, Ankara, 06560, Turkey*

Received 2 August 2007; received in final revised form 25 February 2008

Available online 5 March 2008

Abstract

Based on the theory developed in Part 1 of this paper [Levitas, V.I., Ozsoy, I.B., 2008. Micromechanical modeling of stress-induced phase transformations. Part 1. Thermodynamics and kinetics of coupled interface propagation and reorientation. *Int. J. Plasticity*. doi:10.1016/j.ijplas.2008.02.004], various non-trivial examples of microstructure evolution under complex multiaxial loading are presented. For the case without interface rotation, the effect of the athermal thresholds for austenite (A)–martensite (M) and martensitic variant M_I –variant M_{II} interfaces and loading paths on stress–strain curves and phase transformations was studied. For coupled interface propagation and rotation, two types of numerical simulations were carried out. The tetragonal–orthorhombic transformation has been studied under general three-dimensional interface orientation and zero athermal threshold. The cubic–tetragonal transformation was treated with allowing for an athermal threshold and interface reorientation within a plane. The effect of the athermal threshold, the number of martensitic variants and an interface orientation in the embryo was studied in detail. It was found that an instability in the interface normal leads to a jump-like interface reorientation that has the following features of the energetics of a first-order transformation: there are multiple energy minima versus interface orientation that are separated by an energy barrier; positions of minima do not change during loading but their depth varies; when the barrier disappears (i.e. one of the minima transforms to the local saddle or maximum points), the system rapidly evolves toward another stable orientation. Depending on the loading and material parameters, we observed a large continuous change in interface orientation, a jump in interface reorientation, a jump in volume fractions and

* Corresponding author. Tel.: +1 806 742 3563x244; fax: +1 806 742 3540.
E-mail address: valery.levitas@ttu.edu (V.I. Levitas).

stresses, an expected stress relaxation during the phase transition and unexpected stress growth during the transition because of large change in elastic moduli.

© 2008 Elsevier Ltd. All rights reserved.

Keywords: Phase transformation; Twinning; Constitutive behavior

1. Introduction

In the first part of the paper (Levitas and Ozsoy, 2008), the universal driving force for interface rotation during a coherent phase transformation was derived for small and large strains. Explicit relationships between the rates of interface propagation and interface rotation and the driving forces for interface propagation and interface rotation were obtained. In the current paper, we will apply this theory to specific phase transformation and various complex loadings to study the effect of material parameters, the number of martensitic variants and the type of loading on the coupled evolution of the stresses in phases, macroscopic stresses and crystallographic parameters, including the interface reorientation. For the cases where comparison with previous solutions without an athermal threshold and with experiment was possible, our results are in good agreement. For the numerical study, we did not intend to study a specific phase transformation in a specific material. We studied several rather generic models to find some general properties of the material response and predict interesting phenomena independent of specific material constants. One of the reasons why it is not straightforward to directly compare our calculated stress–strain curves with the experiments is related to the following. We obtained that the macroscopic stress decreases with growing strain during the direct phase transformation under loading and increases during the reverse transformation under unloading. This behavior is caused by internal stresses due to incompatible transformation strain. It will lead to material instability in the solution of a boundary-value problem for a finite sample which will result in the localization of transformation strain and formation of the discrete martensitic microstructure (see Levitas et al., 2004; Idesman et al., 2005). Thus, these micromechanically-based constitutive equations can be used in finite element simulation of the discrete multiconnected martensitic microstructure instead of pure phenomenological models in Levitas et al. (2004) and Idesman et al. (2005). It is known that the force–displacement (averaged stress–averaged strain) curve for a finite sample will be different from the local stress–strain curve in Figs. 2, 3 and 22 due to material instability and heterogeneous fields (see Idesman et al., 2005). Consequently, direct comparison of any unstable constitutive equations with a macroscopic experiment can be done after the solution of boundary-value problems and requires a special procedure.

Another reason to use generic models is that the kinetic equations for interface reorientation and propagation, allowing for athermal friction, were derived in Part 1 for the two-dimensional interface reorientation. In order to ensure the two-dimensional interface reorientation under complex loadings that we study, we have to consider isotropic elasticity. Material parameters are chosen to demonstrate large interface rotation. Since the only reason for the reorientation for a single martensitic variant is change in elastic moduli, we considered large change in Young's modulus. We consider that the product phase has a four times larger elastic modulus (which is typical, for example, for high pressure transformations and has not been studied in detail) or three times smaller Young's modulus like

for NiTi shape memory alloy. Large increase in modulus with relatively small transformation strain leads to a new effect, namely to unexpected stress growth during the direct or reverse transition. This happens because the increase in elastic strains due to change in elastic moduli exceeds their decrease due to transformation strain. The athermal resistance to the interface motion can be varied in a wide range by preliminary plastic deformation or thermomechanical treatment. That is why we varied these thresholds in a wide range.

The paper is organized as follows. In Section 2, we summarize the complete system of equations which describes the problem. In Section 3, some intermediate calculations for stresses, strains, interface length and driving force for interface reorientation are presented. In Section 4, comparison of our analytical solutions for interface orientation with known solutions and available experiments is performed. Parameters for thermodynamically equilibrium embryo are determined in Section 5. In Section 6, the computational algorithms are described. Section 7 contains numerical examples for various types of loading. Concluding remarks are summarized in Section 8.

2. Complete system of equations describing the problem

Let us summarize the complete system of equations derived in Levitas and Ozsoy (2008) for the deformation, phase transformations and interface reorientation in a cube of unit size. The volume consists of austenite A and martensite M divided by a plane interface or multiple interfaces; martensite itself consists of a fine mixture of M_I and M_{II} variants divided by multiple plane interfaces (see Fig. 1 in Levitas and Ozsoy, 2008).

Mixture rules:

$$\boldsymbol{\varepsilon} = c_I \boldsymbol{\varepsilon}_I + c_{II} \boldsymbol{\varepsilon}_{II} + c_A \boldsymbol{\varepsilon}_A; \quad \boldsymbol{\varepsilon}_M = \frac{c_I}{c_M} \boldsymbol{\varepsilon}_I + \frac{c_{II}}{c_M} \boldsymbol{\varepsilon}_{II}; \quad (1)$$

$$\boldsymbol{\sigma} = c_I \boldsymbol{\sigma}_I + c_{II} \boldsymbol{\sigma}_{II} + c_A \boldsymbol{\sigma}_A; \quad \boldsymbol{\sigma}_M = \frac{c_I}{c_M} \boldsymbol{\sigma}_I + \frac{c_{II}}{c_M} \boldsymbol{\sigma}_{II}. \quad (2)$$

Here $\boldsymbol{\sigma}$ and $\boldsymbol{\varepsilon}$ are the stress and strain tensors averaged over the entire cube, subscripts A, M, I and II designate the austenite, martensite and first and second martensitic variants, respectively, c is for the volume fractions of corresponding phase or martensitic variant.

Kinematic decompositions:

$$\boldsymbol{\varepsilon} = \boldsymbol{\varepsilon}_e + \boldsymbol{\varepsilon}_t; \quad \boldsymbol{\varepsilon}_I = \boldsymbol{\varepsilon}_{eI} + \boldsymbol{\varepsilon}_{tI}; \quad \boldsymbol{\varepsilon}_{II} = \boldsymbol{\varepsilon}_{eII} + \boldsymbol{\varepsilon}_{tII}; \quad \boldsymbol{\varepsilon}_A = \boldsymbol{\varepsilon}_{eA}; \quad (3)$$

where subscripts t and e are for the transformation and elastic strains.

Hooke's laws:

$$\boldsymbol{\sigma}_I = \mathbf{E}_I : (\boldsymbol{\varepsilon}_I - \boldsymbol{\varepsilon}_{tI}); \quad \boldsymbol{\sigma}_{II} = \mathbf{E}_{II} : (\boldsymbol{\varepsilon}_{II} - \boldsymbol{\varepsilon}_{tII}); \quad \boldsymbol{\sigma}_A = \mathbf{E}_A : \boldsymbol{\varepsilon}_A; \quad \boldsymbol{\sigma}_M = \mathbf{E}_M : (\boldsymbol{\varepsilon}_M - \boldsymbol{\varepsilon}_{tM}); \quad (4)$$

where \mathbf{E} with corresponding subscripts are the fourth-rank elasticity tensors of each phase or martensitic variant.

Hadamard compatibility conditions:

$$\boldsymbol{\varepsilon}_M - \boldsymbol{\varepsilon}_A = (\mathbf{a}\mathbf{n})_s; \quad \boldsymbol{\varepsilon}_{II} - \boldsymbol{\varepsilon}_I = (\mathbf{a}_I \mathbf{n}_I)_s. \quad (5)$$

Here \mathbf{n} and \mathbf{n}_I are the normals to the A–M interface and M_I – M_{II} interfaces, \mathbf{a} and \mathbf{a}_I are the vectors characterizing the jumps in strains across these interfaces and the subscript s denotes the symmetrization.

Traction continuity conditions:

$$\boldsymbol{\sigma}_A \cdot \mathbf{n} = \boldsymbol{\sigma}_M \cdot \mathbf{n}; \quad \boldsymbol{\sigma}_I \cdot \mathbf{n}_I = \boldsymbol{\sigma}_{II} \cdot \mathbf{n}_I. \quad (6)$$

Driving forces for A–M and M_I – M_{II} interface reorientation:

$$\mathbf{X}_n := -c_A c_M \mathbf{a} \cdot (\boldsymbol{\sigma}_M - \boldsymbol{\sigma}_A), \quad (7)$$

$$\mathbf{X}_n^I := -\frac{c_I c_{II}}{c_M^2} \mathbf{a}_I \cdot (\boldsymbol{\sigma}_{II} - \boldsymbol{\sigma}_I). \quad (8)$$

Driving forces for A–M and M_I – M_{II} interface propagation:

$$X_c = 0.5(\boldsymbol{\sigma}_A + \boldsymbol{\sigma}_M) : \boldsymbol{\varepsilon}_M^t - 0.5\boldsymbol{\varepsilon}_A^e : (\mathbf{E}_M - \mathbf{E}_A) : \boldsymbol{\varepsilon}_M^e - (\psi_M^\theta - \psi_A^\theta), \quad (9)$$

$$X_c^I := 0.5(\boldsymbol{\sigma}_I + \boldsymbol{\sigma}_{II}) : (\boldsymbol{\varepsilon}_{II} - \boldsymbol{\varepsilon}_{II}^I) - 0.5\boldsymbol{\varepsilon}_I^e : (\mathbf{E}_{II} - \mathbf{E}_I) : \boldsymbol{\varepsilon}_{II}^e. \quad (10)$$

In our examples, we assume $\mathbf{E}_I = \mathbf{E}_{II}$.

Kinetic equations and phase transformation criteria:

(a) Three-dimensional loading without interface rotation

$$\begin{aligned} \dot{c}_M &= \frac{\Sigma}{\lambda V} (X_c - k) \quad \text{for } X_c > k; \\ \dot{c}_M &= \frac{\Sigma}{\lambda V} (X_c + k) \quad \text{for } X_c < -k; \\ \dot{c}_M &= 0 \quad \text{for } |X_c| \leq k. \end{aligned} \quad (11)$$

$$\begin{aligned} \dot{c}_{II \rightarrow I} &= h^I (X_c^I - k^I) \quad \text{for } X_c^I > k^I; \\ \dot{c}_{II \rightarrow I} &= h^I (X_c^I + k^I) \quad \text{for } X_c^I < -k^I; \\ \dot{c}_{II \rightarrow I} &= 0 \quad \text{for } |X_c^I| \leq k^I. \end{aligned} \quad (12)$$

$$\dot{c}_{II} = \dot{c}_{A \rightarrow II} - \dot{c}_{II \rightarrow I} = \dot{c}_M \frac{c_{II}}{c_M} - \dot{c}_{II \rightarrow I}, \quad (13)$$

$$\dot{c}_I = \dot{c}_{A \rightarrow I} + \dot{c}_{II \rightarrow I} = \dot{c}_M \frac{c_I}{c_M} + \dot{c}_{II \rightarrow I} = \dot{c}_M - \dot{c}_{II}, \quad (14)$$

where k is the athermal interface friction, λ is the viscosity coefficient, Σ is the total area of all interfaces, h^I is the kinetic constant, and $V = 1$ is the volume of the cube. In Eqs. (13) and (14) one takes into account that the volume fraction of each martensitic variant changes because of variant–variant transformation and phase transformation $A \rightarrow M$. The rate of phase transformation from A to each variant is proportional to the fraction of this variant.

(b) Three-dimensional interface reorientation and propagation with $k = k^I = 0$

$$\dot{c}_M = \frac{\Sigma}{\lambda V} X_c, \quad (15)$$

$$\dot{c}_{II} = \dot{c}_{A \rightarrow II} - \dot{c}_{II \rightarrow I} = \dot{c}_M \frac{c_{II}}{c_M} - \dot{c}_{II \rightarrow I}, \quad (16)$$

$$\dot{c}_I = \dot{c}_{A \rightarrow I} + \dot{c}_{II \rightarrow I} = \dot{c}_M \frac{c_I}{c_M} + \dot{c}_{II \rightarrow I} = \dot{c}_M - \dot{c}_{II}, \quad (17)$$

$$\dot{c}_{II \rightarrow I} = h^I X_c^I, \quad (18)$$

$$\dot{\mathbf{n}} = h_n \mathbf{X}_n; \quad \dot{\mathbf{n}}_I = h_{nI} \mathbf{X}_n^I. \quad (19)$$

- (c) Two-dimensional reorientation and propagation of the A–M interface with $k \neq 0$, $k^I = 0$

$$\begin{aligned} \dot{c}_M &= v_{0n} \Sigma / V = 2\omega_0 R^2 = 2R^2 g_3 / (3C); \\ \dot{\varphi} &= 2^{2/3} g_3 g_4 / C \quad \text{for } \tilde{X}_c - 3\tilde{X}_n \leq 2; \end{aligned} \quad (20)$$

$$\begin{aligned} \dot{c}_M &= 2R^2 (\tilde{X}_c - 2) / (3C); \\ \dot{\varphi} &= \tilde{X}_n / C \quad \text{for } \tilde{X}_c - 3\tilde{X}_n > 2; \end{aligned} \quad (21)$$

where

$$\tilde{X}_c = X_c R \Sigma / (AV); \quad \tilde{X}_n = X_n / A, \quad (22)$$

$$\begin{aligned} g_1 &= (9\tilde{X}_c + (81\tilde{X}_c^2 + 4(3\tilde{X}_n - 1)^3)^{1/2})^{1/3}; \quad g_2 = 2 - 6\tilde{X}_n + 2^{1/3} g_1^2; \\ g_3 &= \tilde{X}_c - 2^{1/3} / (3g_4); \quad g_4 = g_1 / g_2; \\ A &= kR^2 / S; \quad C := B / A; \quad B = 2\lambda R^3 / (3S). \end{aligned} \quad (23)$$

Here $2R$ is the interface length, v_{0n} is the velocity of translational motion of the interface, φ is the angle between the normal to the A–M interface and direction 1 (i.e. $n_1 = \cos \varphi$), $\omega_0 = v_{0n} / R$ and $S = 1$ is the area of the cube face.

$$\dot{c}_{II} = \dot{c}_{A \rightarrow II} - \dot{c}_{II \rightarrow I} = \dot{c}_M \frac{c_{II}}{c_M} - \dot{c}_{III}; \quad (24)$$

$$\dot{c}_I = \dot{c}_{A \rightarrow I} + \dot{c}_{II \rightarrow I} = \dot{c}_M \frac{c_I}{c_M} + \dot{c}_{II \rightarrow I} = \dot{c}_M - \dot{c}_{II}; \quad (25)$$

$$\dot{c}_{II \rightarrow I} = h^I X_c^I. \quad (26)$$

The above equations are coupled and have to be solved together.

3. Calculations of stresses, strains, interface length and driving force for interface reorientation

In this section, we will present some intermediate calculations.

3.1. Prescribed strains

When the strains $\boldsymbol{\varepsilon}$ are prescribed, the following equations are obtained by using the Hooke's law (4), the Hadamard compatibility equation (5) and the traction continuity equation (6):

$$\mathbf{n} \cdot \mathbf{E}_A : (\boldsymbol{\varepsilon} - c_M (\mathbf{a}\mathbf{n})_s) = \mathbf{n} \cdot \mathbf{E}_M : (\boldsymbol{\varepsilon} + c_A (\mathbf{a}\mathbf{n})_s - \boldsymbol{\varepsilon}_{tM}), \quad (27)$$

$$\begin{aligned} \mathbf{n}_I \cdot \mathbf{E}_I : (\boldsymbol{\varepsilon} + c_A (\mathbf{a}\mathbf{n})_s - c_{II} / c_M (\mathbf{a}_I \mathbf{n}_I)_s - \boldsymbol{\varepsilon}_{tI}) \\ = \mathbf{n}_I \cdot \mathbf{E}_{II} : (\boldsymbol{\varepsilon} + c_A (\mathbf{a}\mathbf{n})_s + c_I / c_M (\mathbf{a}_I \mathbf{n}_I)_s - \boldsymbol{\varepsilon}_{tII}). \end{aligned} \quad (28)$$

They can be solved for a given \mathbf{n} and \mathbf{n}_I for the vectors \mathbf{a} and \mathbf{a}_I . Then, the strains and stresses in the phases and the ones averaged over the martensite can be found from Eqs. (4) and (5):

$$\boldsymbol{\varepsilon}_A = \boldsymbol{\varepsilon} - c_M (\mathbf{a}\mathbf{n})_s; \quad \boldsymbol{\varepsilon}_M = \boldsymbol{\varepsilon} + c_A (\mathbf{a}\mathbf{n})_s; \quad \boldsymbol{\varepsilon}_{tM} = c_I \boldsymbol{\varepsilon}_{tI} + c_{II} \boldsymbol{\varepsilon}_{tII}; \quad (29)$$

$$\begin{aligned} \boldsymbol{\varepsilon}_I &= \boldsymbol{\varepsilon} + c_A (\mathbf{a}\mathbf{n})_s - c_{II} / c_M (\mathbf{a}_I \mathbf{n}_I)_s; \\ \boldsymbol{\varepsilon}_{II} &= \boldsymbol{\varepsilon} + c_A (\mathbf{a}\mathbf{n})_s + c_I / c_M (\mathbf{a}_I \mathbf{n}_I)_s; \end{aligned} \quad (30)$$

$$\boldsymbol{\sigma}_A = \mathbf{E}_A : (\boldsymbol{\varepsilon} - c_M(\mathbf{a}\mathbf{n})_s); \quad \boldsymbol{\sigma}_M = \mathbf{E}_M : (\boldsymbol{\varepsilon} + c_A(\mathbf{a}\mathbf{n})_s - \boldsymbol{\varepsilon}_{tM}); \quad (31)$$

$$\boldsymbol{\sigma}_I = \mathbf{E}_I : (\boldsymbol{\varepsilon} + c_A(\mathbf{a}\mathbf{n})_s - c_{II}/c_M(\mathbf{a}_I\mathbf{n}_I)_s - \boldsymbol{\varepsilon}_{tI});$$

$$\boldsymbol{\sigma}_{II} = \mathbf{E}_{II} : (\boldsymbol{\varepsilon} + c_A(\mathbf{a}\mathbf{n})_s + c_I/c_M(\mathbf{a}_I\mathbf{n}_I)_s - \boldsymbol{\varepsilon}_{tII}). \quad (32)$$

3.2. Prescribed stresses $\boldsymbol{\sigma}$

The same problem can be solved for prescribed stresses $\boldsymbol{\sigma}$, using the local coordinate system in which $\mathbf{n}^* = (1, 0, 0)$. The rotation matrix \mathbf{m} is described by the three Eulerian angles z_1, z_2, z_3 , where we put $z_1 = 0$ without loss of generality, i.e.

$$\mathbf{m} = \begin{pmatrix} \cos z_3 & \cos z_2 \sin z_3 & \sin z_3 \sin z_2 \\ -\sin z_3 & \cos z_2 \cos z_3 & \cos z_3 \sin z_2 \\ 0 & -\sin z_2 & \cos z_2 \end{pmatrix}.$$

Solving the equation $\mathbf{m} \cdot \mathbf{n} = (1, 0, 0)$ together with $n_1^2 + n_2^2 + n_3^2 = 1$ for x and z_2 , where $\mathbf{n} = (n_1, n_2, n_3)$ is the normal in the global coordinate system, we find that the rotation matrix \mathbf{m} is

$$\mathbf{m} = \begin{pmatrix} n_1 & n_2 & \text{sign}(n_3)n_3 \\ -\sqrt{1-n_1^2} & \frac{n_1n_2}{\sqrt{n_2^2+n_3^2}} & \text{sign}(n_3)n_1\sqrt{\frac{1-n_2^2}{n_2^2+n_3^2}} \\ 0 & -\text{sign}(n_3)\sqrt{\frac{n_3^2}{n_2^2+n_3^2}} & \frac{n_2}{\sqrt{n_2^2+n_3^2}} \end{pmatrix}. \quad (33)$$

To find components of the stress $\boldsymbol{\sigma}_i$ and transformation strain tensors $\boldsymbol{\varepsilon}_{ti}$ and fourth-rank compliance tensors $\mathbf{C}_i = \mathbf{E}_i^{-1}$ in the local coordinate system, they are rotated by the rotation matrix \mathbf{m} using $C_{ijkl} = m_{im}m_{jn}m_{ko}m_{lp}C'_{mnop}$, $\sigma_i^{mn} = m_{mk}m_{nl}\sigma_i^{kl'}$, $\varepsilon_{ti}^{mn} = m_{mk}m_{nl}\varepsilon_{ti}^{kl'}$, where the components of the tensors in the local and global coordinates are without and with prime, respectively. Then, from the traction continuity equation $\boldsymbol{\sigma}_A \cdot \mathbf{n} = \boldsymbol{\sigma}_M \cdot \mathbf{n} = \boldsymbol{\sigma} \cdot \mathbf{n}$, one can find the stress components in the phases as $\sigma_A^{11} = \sigma_M^{11} = \sigma^{11}$, $\sigma_A^{12} = \sigma_M^{12} = \sigma^{12}$ and $\sigma_A^{13} = \sigma_M^{13} = \sigma^{13}$. Inserting $\boldsymbol{\varepsilon}_M = \mathbf{C}_M : \boldsymbol{\sigma}_M + \boldsymbol{\varepsilon}_M^t$ and $\boldsymbol{\varepsilon}_A = \mathbf{C}_A : \boldsymbol{\sigma}_A$ into the Hadamard compatibility equation, we obtain $\mathbf{C}_M : \boldsymbol{\sigma}_M - \mathbf{C}_A : \boldsymbol{\sigma}_A + \boldsymbol{\varepsilon}_M^t = (\mathbf{a}\mathbf{n})_s$. Solving this equation, the vector \mathbf{a} and stress components σ_A^{22} , σ_A^{23} and σ_A^{33} in the phases are found. The remaining stress components σ_M^{22} , σ_M^{23} and σ_M^{33} in martensite can be calculated by solving the equations

$$\sigma^{22} = c_A\sigma_A^{22} + c_M\sigma_M^{22}, \quad \sigma^{23} = c_A\sigma_A^{23} + c_M\sigma_M^{23}, \quad \sigma^{33} = c_A\sigma_A^{33} + c_M\sigma_M^{33}.$$

Then, the stresses $\boldsymbol{\sigma}_i$ and vector \mathbf{a} are rotated back to the global coordinate system by using \mathbf{m}^{-1} , and the strains $\boldsymbol{\varepsilon}_i$ in phases are found in the global coordinate system by using the equations $\boldsymbol{\varepsilon}_A = \mathbf{C}_A : \boldsymbol{\sigma}_A$ and $\boldsymbol{\varepsilon}_M = \mathbf{C}_M : \boldsymbol{\sigma}_M + \boldsymbol{\varepsilon}_{tM}$.

Since the strains in martensite are now known, the vector \mathbf{a}_I , the stresses $\boldsymbol{\sigma}_I$, $\boldsymbol{\sigma}_{II}$, and strains $\boldsymbol{\varepsilon}_I$, $\boldsymbol{\varepsilon}_{II}$ in the martensitic variants are found by using the procedure from Section 3.1 when the strains are prescribed. Tensors \mathbf{E}_M and \mathbf{C}_M are can be taken from [Stupkiewicz and Petryk \(2002\)](#).

3.3. Mixed boundary conditions

When the mixed boundary conditions are given, e.g. uniaxial loading and biaxial loading (one or two strain components are prescribed and the stress components in the other

directions are zero), the macroscopic strains can be found (directly or iteratively) to produce the required boundary conditions. Some are given below.

Uniaxial loading. When the material is isotropic and there is no difference between the elastic moduli E_i of the phases, the relation between the elastic strains are found easily by using the Hooke's law. The relation between the stresses and strains for isotropic materials are

$$\begin{aligned} \varepsilon_{11}^e &= \frac{1}{E} [(1 + \nu)\sigma_{11} - \nu(\sigma_{11} + \sigma_{22} + \sigma_{33})]; \\ \varepsilon_{22}^e &= \frac{1}{E} [(1 + \nu)\sigma_{22} - \nu(\sigma_{11} + \sigma_{22} + \sigma_{33})]; \\ \varepsilon_{33}^e &= \frac{1}{E} [(1 + \nu)\sigma_{33} - \nu(\sigma_{11} + \sigma_{22} + \sigma_{33})]; \\ \varepsilon_{12}^e &= \frac{1 + \nu}{E} \sigma_{12}; \quad \varepsilon_{13}^e = \frac{1 + \nu}{E} \sigma_{13}; \quad \varepsilon_{23}^e = \frac{1 + \nu}{E} \sigma_{23}; \end{aligned} \tag{34}$$

where E and ν are the elasticity modulus and the Poisson's ratio. Inserting the condition for uniaxial stresses $\sigma_{11} \neq 0$, $\sigma_{22} = \sigma_{33} = \sigma_{12} = \sigma_{13} = \sigma_{23} = 0$ into Eq. (34) we obtain

$$\varepsilon_{22}^e = \varepsilon_{33}^e = -\nu\varepsilon_{11}^e \tag{35}$$

for prescribed strain component ε_{11} . Since $\boldsymbol{\varepsilon} = \boldsymbol{\varepsilon}^e + \boldsymbol{\varepsilon}^t$, where $\boldsymbol{\varepsilon}^t = c_M \boldsymbol{\varepsilon}_{tM}$, we can find the elastic strains from the following equations:

$$\varepsilon_{11}^e = \varepsilon_{11} - c_M \varepsilon_{11}^{tM}; \quad \varepsilon_{22}^e = \varepsilon_{33}^e = -\nu\varepsilon_{11}^e. \tag{36}$$

Then, the strain components which give the uniaxial stress condition are found as

$$\varepsilon_{22} = \varepsilon_{22}^e + c_M \varepsilon_{22}^{tM}; \quad \varepsilon_{33} = \varepsilon_{33}^e + c_M \varepsilon_{33}^{tM}. \tag{37}$$

These strains have to be updated iteratively with c_M and $\boldsymbol{\varepsilon}_{tM}$ at each time integration step.

For isotropic material with different Young's moduli of the phases, E_A and E_M , using Eqs. (1) and (2) and (34), and applying some algebra, we obtain

$$\begin{aligned} \varepsilon_{22} &= \frac{-\nu\sigma_{11}}{E_M} + \frac{E_M - E_A}{E_M} c_A \varepsilon_{22}^A + c_M \varepsilon_{22}^{tM}; \\ \varepsilon_{33} &= \frac{-\nu\sigma_{11}}{E_M} + \frac{E_M - E_A}{E_M} c_A \varepsilon_{33}^A + c_M \varepsilon_{33}^{tM}. \end{aligned} \tag{38}$$

Biaxial loading: To prescribe strains for biaxial stresses, we need to find the strain ε_{22} for $\sigma_{11} \neq 0$, $\sigma_{33} \neq 0$ and $\sigma_{22} = \sigma_{12} = \sigma_{13} = \sigma_{23} = 0$. Using Eq. (34), we obtain

$$\varepsilon_{22} = -\frac{\nu}{E} (\sigma_{11} + \sigma_{33}) + c_M \varepsilon_{22}^{tM}. \tag{39}$$

3.4. Calculation of the interface length in two dimensions

With the known angle φ between the axis 1 and the normal to the interface and the volume fraction c_M , one can find the interface length, $2R$ (Fig. 1). The volume fraction c_M is equal to the area of the part of the square below the interface. When the interface intersects the sides S_1 and S_4 of the unit cube, the maximum volume fraction of the martensitic phase is bounded by line I. For line I, $c_M = 1/(2 \tan \varphi)$. When the interface intersects S_2

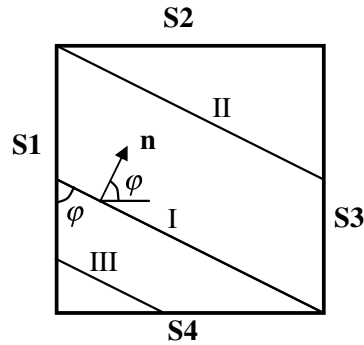


Fig. 1. The scheme of a unit cube for the calculation of the interface length. Lines I and II divide the surface into three sections where the expressions for interface lengths should be found for a given volume fraction c_M .

and S_3 , line II bounds the volume fraction c_M at the minimum value, which is $c_{II} = 1 - 1/(2 \tan \varphi)$. So, the expression for the interface length should be found for the following three regions of the cube:

1. For $c_M < 1/(2 \tan \varphi)$ (the interface is below line I). Since $c_M = 2R \cos \varphi / 2R \sin \varphi / 2$, then $2R = \sqrt{2c_M / (\cos \varphi \sin \varphi)}$.
2. For $1/(2 \tan \varphi) \leq c_M \leq 1 - 1/(2 \tan \varphi)$ (the interface is between line I and line II). For this case, the interface length is equal the length of line I which is $2R = 1 / \sin \varphi$.
3. For $c_M > 1 - 1/(2 \tan \varphi)$; (the interface is above line II). Using similar relations as in case 1, the interface length is expressed as $2R = \sqrt{2(1 - c_M) / (\cos \varphi \sin \varphi)}$.

3.5. Calculation of driving force for interface rotation

The magnitude of X_n in the equation $\mathbf{X}_n \cdot \dot{\mathbf{n}} = X_n \dot{\varphi}$ (Levitas and Ozsoy, 2008) is equal to the magnitude of \mathbf{X}_n , which is $|\mathbf{X}_n| = \sqrt{X_{n1}^2 + X_{n2}^2}$.

The problem here is finding the sign of the X_n . Since \mathbf{X}_n and \mathbf{n} are mutually orthogonal, the following procedure is used. First, the driving force for interface rotation, \mathbf{X}_n , is rotated 90° clockwise, which yields $\mathbf{X}'_n = (X_{n2}, -X_{n1})$, where \mathbf{X}'_n is the rotated driving force. Then it is projected into \mathbf{n} , i.e. $X_n = \mathbf{X}'_n \cdot \mathbf{n}$ is found which gives $X_n = X_{n2}n_1 - X_{n1}n_2 = X_{n2} \cos \varphi - X_{n1} \sin \varphi$.

4. Comparison with known solutions and experiments

Using the explicit expressions for stresses and strains in the phases from Section 4.3 in Levitas and Ozsoy (2008), phase and orientational equilibrium configurations can be determined from the conditions $X_c = X_n = 0$ for $k = 0$. First, a comparison was made with results for the case without the stresses (crystallographic theory) summarized in Bhattacharya (2004). For any cubic to tetragonal phase transformation, and cubic to orthorhombic transformation, the results are the same as the analytical solutions given in Bhattacharya (2004). For cubic to orthorhombic transformation with the variants which form compound twins (e.g. variants 1 and 2), we can not obtain an austenite martensite interface in any of our calculations, which is also stated in Bhattacharya (2004).

Assuming phases with equal isotropic elastic moduli, we obtained analytic solutions for cubic–tetragonal and tetragonal–orthorhombic phase transformations. These solutions coincide with those presented in Roytburd and Kosenko (1976) for the cases of single martensitic variant and the mixture of two martensitic variants. Solutions have been obtained under multiaxial loading by normal stresses (strains) along cubic directions. For uniaxial tension and compression, there is also a coincidence with Roytburd and Slutsker's solutions (2001) for cubic to tetragonal phase transformation, when internal stresses are involved. Since these solutions are in reasonable agreement with experiments in Pankova and Roytburd (1984), the same can be expected from our equations for more complex loading.

Note that for tetragonal–orthorhombic phase transformation, Roytburd and Kosenko (1976) assumed that normal to interface belongs to one of the crystallographic planes, otherwise solutions could not be obtained. We found this analytical solution without the assumption but obtained the same result.

It is useful to analyze analytical solutions to find out for which loading program one may expect a large change in interface orientation. For cubic–tetragonal phase transformation, the components of the normal $\mathbf{n} = (n_1, n_2, n_3)$ are

$$n_1^2 = \frac{(y + v) + (1 + vy)x}{x - 1}; \quad n_2^2 = 1 - n_1^2; \quad n_3^2 = 0; \quad (40)$$

where $x = \varepsilon_I^t / \varepsilon_{II}^t$ and $y = c_{II} / c_I$. Here, we use the material parameters for the In–23 at.% Tl: $x = 0.0221 / (-0.0111) = -2$ and $v = 0.3$. By analyzing the function $n_1(y)$, we found that as y approaches 4, the normal orientation changes significantly. Since y depends on the external stresses, we can design a loading process in order to have such a volume fraction ratio and observe the large change in the normal.

5. Determination of the parameters for thermodynamically equilibrium embryo

By definition, the thermodynamically equilibrium embryo is placed at the corner of the parallelepiped and separated by a plane interface; it possesses minimum Gibbs energy under prescribed stress σ or minimum of elastic energy under prescribed strain ε . That means that the orientation of its interface and interface between martensitic variants, as well as concentrations of martensitic variants c_I and c_{II} are determined from the thermodynamic equilibrium conditions

$$X_n = 0; \quad X_n^I = 0; \quad X_c^I = 0. \quad (41)$$

To guarantee that the embryo's parameters correspond to the minimum of the energy (rather than the stationary value), we apply permanently small perturbations and solve for $c_M = \text{const}$ the kinetic equations

$$\dot{c}_I = h_{cI} X_c^I; \quad \dot{\mathbf{n}} = h_n X_n; \quad \dot{\mathbf{n}}_I = h_{nI} X_n^I \text{ for martensitic embryo,} \quad (42)$$

$$\dot{\mathbf{n}} = h_n X_n \text{ for austenitic embryo,} \quad (43)$$

until the stationary solution is reached. When an external stress is applied, the selection of the first and second variant among all possible variants is based on maximization of the thermodynamic driving force X_c in Eq. (9) with respect to ε_{ij} . For the temperature-induced phase transformation, any variant can be taken as the first one. Then internal stresses will

select the second variant as for stress-induced phase transformation. We do not need to repeat calculations for other choices of the first variant, the results are clear from the symmetry consideration.

When one starts with pure austenite (or martensite), the possibility of martensite (or austenite) nucleation has to be checked at each time step. It includes the determination of thermodynamically equilibrium parameters of an embryo, c_I/c_{II} , \mathbf{n} and \mathbf{n}_I for martensitic nucleus and normal \mathbf{n} for austenitic nucleus and checking the phase transformation criterion equation (11) with $k > 0$ (Levitas et al., 2007). To do this, when the initial condition is $c_M = 0$, we include artificially a very small amount of martensite ($c_M = 0.0002$) as an initial condition with $c_I = 0.0001$ and some \mathbf{n} and \mathbf{n}_I . The effect of these numbers on the final result is very small, because they produce only 0.02% and 0.01% error, which is acceptable for a numerical solution. The thermodynamically equilibrium characteristics of the embryo, c_I , \mathbf{n} and \mathbf{n}_I , are determined for each time step by the integration of Eq. (42) with $k = k_I = 0$, until the stationary solutions for these parameters are reached. Consequently, one needs to introduce one more time-like variable for the embryo (fast time), which varies when the real (slow) time is fixed.

When the phase transformation criterion, allowing for interface friction, is met, the embryo becomes a nucleus and calculations with $k \geq 0$ and $k_I \geq 0$ are continued according to Eqs. (11) and (12) or Eq. (21). We also include the condition that if $c_M < 0.0002$ and $\dot{c}_M < 0$ at the end of each loading step (i.e. if the phase transformation criterion is not satisfied), then we set $c_M = 0.0002$ and $\dot{c}_M = 0$. This prevents the disappearance of the embryo.

A similar procedure is performed for the initial condition $c_A = 0$. We put $c_M = 0.9998$ and obtain the thermodynamically equilibrium \mathbf{n} by integrating Eq. (43) over fast time. After nucleation, we do not allow c_M to be larger than 0.9998.

For some initial conditions for \mathbf{n} and \mathbf{n}_I , stationary solutions for \mathbf{n} and \mathbf{n}_I may correspond to a maximum or saddle point of free energy rather than to a minimum. Despite the fact that these equilibrium values are unstable, the system may stack in it. To avoid this, the following procedure was used. First, we find all possible \mathbf{n} and \mathbf{n}_I from algebraic equations $|\mathbf{X}_n| = |\mathbf{X}_{nI}| = 0$. Then we chose those \mathbf{n} and \mathbf{n}_I which correspond to a minimum of free energy. In general, we prescribed a small perturbation to the normals to avoid eventual stacking in points corresponding to energy saddle or maximum points.

Assume that all material properties (\mathbf{E}_I , \mathbf{E}_{II} , \mathbf{E}_A , $\boldsymbol{\varepsilon}_{II}$, $\boldsymbol{\varepsilon}_{III}$) are known; macroscopic strain $\boldsymbol{\varepsilon}$ and temperature (i.e. $\Delta\psi^\theta$) are prescribed. The volume fractions of each phase and variants, c_A and c_I , and the orientation of the austenite–martensite phases and variant–variant interfaces, \mathbf{n} and \mathbf{n}_I , can be found at each time step by solution of evolution equations (11), (12) and (19). Then the vectors \mathbf{a} and \mathbf{a}_I which are characterizing the jump in strain across the A–M interface and variant–variant interface can be found by solving Eqs. (27) and (28) at the same time steps. Substituting the vectors \mathbf{a} and \mathbf{a}_I into Eqs. (29) and (30), the strains in M_I , M_{II} , A , and M are obtained. Substituting these strain values into the Hooke's law, the stresses in M_I , M_{II} , A , and M are obtained. The same procedure is repeated for the next time step.

6. Computational algorithm

A computational algorithm is developed to effectively solve the above system of differential and algebraic equations and used for the numerical study of stress-induced transfor-

mations. We consider both stationary solutions for each loading step and non-stationary solutions (kinetic loading).

6.1. Algorithm for calculations for 3D interface (with and without interface rotation, i.e. case a and b)

1. Initiate embryo

$$c_I = c_{II} = 0.0001, \text{ arbitrary } \mathbf{n}, \mathbf{n}_I$$

(for reverse phase transformation, $c_A = 0.0001$)

PT = 0 (no A–M transformation)

2. Apply the load increment, $p = 0$ (prescribe strains $\boldsymbol{\varepsilon}$)

- (a) Calculate \mathbf{a}, \mathbf{a}_I from Eqs. (27) and (28).
- (b) Calculate $\boldsymbol{\varepsilon}_I, \boldsymbol{\varepsilon}_{II}, \boldsymbol{\varepsilon}_A, \boldsymbol{\varepsilon}_M$ by using Eqs. (29) and (30).
- (c) Calculate $\boldsymbol{\sigma}_I, \boldsymbol{\sigma}_{II}, \boldsymbol{\sigma}_A, \boldsymbol{\sigma}_M$ by using Eqs. (31) and (32).
- (d) Calculate $\mathbf{X}_n, \mathbf{X}_n^I, X_c, X_c^I$ from Eqs. (7)–(10).
- (e) Calculate $\dot{c}_M, \dot{c}_I, \dot{\mathbf{n}}$ and $\dot{\mathbf{n}}_I$ using the following procedure:

IF (PT = 0) THEN

$$\dot{c}_M = 0$$

$$\dot{c}_I = h_2 X_c^I$$

ELSE calculate \dot{c}_M and $\dot{c}_{II \rightarrow I}$ from Eqs. (11) and (12)

IF (($c_M < 0$) AND ($X_c < 0$)) THEN $\dot{c}_A = 0$

IF (($c_A < 0$) AND ($X_c > 0$)) THEN $\dot{c}_A = 0$

Find $\dot{c}_{A \rightarrow I}$ and $\dot{c}_{A \rightarrow II}$ from

$$\dot{c}_{A \rightarrow I} = -\dot{c}_A (c_I / (c_I + c_{II}))$$

$$\dot{c}_{A \rightarrow II} = c_{II} / c_I \dot{c}_{A \rightarrow I}$$

IF (($c_{II} < 0$) AND ($X_c^I > 0$)) THEN $\dot{c}_{II \rightarrow I} = 0$

IF (($c_I < 0$) AND ($X_c^I < 0$)) THEN $\dot{c}_{2 \rightarrow 1} = 0$

Find \dot{c}_I from the equation

$$\dot{c}_I = \dot{c}_{II \rightarrow I} + \dot{c}_{A \rightarrow I}$$

- (f) Calculate $\dot{\mathbf{n}}$ and $\dot{\mathbf{n}}_I$ from

$$\dot{\mathbf{n}} = h_3 \mathbf{X}_n$$

$$\dot{\mathbf{n}}_I = h_4 \mathbf{X}_n^I$$

3. Calculate new values for $c_I, c_{II}, c_A, \mathbf{n}, \mathbf{n}_I$ using the simplest predictor–corrector method,

$$p = p + 1$$

$$y_{n+1}^p = y_n + hf(y_n, t_n)$$

IF ($p = 1$) GOTO (2a)

ELSE $y_{n+1}^c = y_n + \frac{h}{2} [f(y_{n+1}^p, t_{n+1}) + f(y_n, t_n)]$

Replace y by $c_I, c_A, \mathbf{n}_I, \mathbf{n}$,

IF ($c_A < 0$) THEN $c_A = 0.000001$

IF ($c_A > 1$) THEN $c_A = 0.999998$

IF ($c_I < 0$) THEN $c_I = 0.000001$

IF ($c_I > 1$) THEN $c_I = 0.999998$

Calculate c_{II} from $c_{II} = 1 - c_A - c_I$

4. IF (kinetic loading) AND PT = 1 GOTO 2

ELSE check convergence for normal and volume fractions (stationary values).

IF TOL > (value) GOTO (2a)

ELSE check PT criteria

IF ($X_c > 0$) THEN PT = 1 (start A–M transformation in the next step)

($X_c < 0$ for reverse PT)

GOTO 2 (next load increment)

6.2. Algorithm for calculations for 2D interface (with interface rotation)

1. Initiate embryo

$c_I = c_{II} = 0.0001$, arbitrary \mathbf{n}, \mathbf{n}_I .

For thermodynamically non-equilibrium embryo, keep \mathbf{n} constant.

PT = 0 (no A–M transformation)

2. Apply the load increment, $p = 0$ (prescribe strains $\boldsymbol{\varepsilon}$)

(a) Calculate \mathbf{a}, \mathbf{a}_I from Eqs. (27) and (28).

(b) Calculate $\boldsymbol{\varepsilon}_I, \boldsymbol{\varepsilon}_{II}, \boldsymbol{\varepsilon}_A, \boldsymbol{\varepsilon}_M$ by using Eqs. (29) and (30).

(c) Calculate $\boldsymbol{\sigma}_I, \boldsymbol{\sigma}_{II}, \boldsymbol{\sigma}_A, \boldsymbol{\sigma}_M$ by using Eqs. (31) and (32).

(d) Calculate X_n, X_n^I, X_c, X_c^I from Eqs. (7)–(10).

(e) Find R (interface length).

$$2R = \sqrt{2c_M / (\cos \varphi \sin \varphi)} \quad \text{if } c_M < 1 / (2 \tan \varphi)$$

$$2R = 1 / \sin \varphi \quad \text{if } 1 / (2 \tan \varphi) \leq c_M \leq 1 - 1 / (2 \tan \varphi)$$

$$2R = \sqrt{2(1 - c_M) / (\cos \varphi \sin \varphi)} \quad \text{if } c_M > 1 - 1 / (2 \tan \varphi)$$

(f) Find \tilde{X}_c and \tilde{X}_n from

$$\tilde{X}_c = 2X_c / k \quad \text{and} \quad \tilde{X}_n = (X_{n2} \cos \varphi - X_{n1} \sin \varphi) / (kR^2)$$

(g) IF PT = 1 (phase transformation started), assume \tilde{X}_c and \tilde{X}_n are both positive and then calculate ω and ω_0 using Eqs. (22) and (21) (in the first quadrant of phase transformation surface)

$$\bar{X}_c = |\tilde{X}_c|, \quad \bar{X}_n = |\tilde{X}_n|,$$

$$\omega_0^a = (\bar{X}_c - 2) / (3C), \quad \omega^a = \bar{X}_n / C,$$

$$\omega_0^b = g_3 / (3C), \quad \omega^b = 2^{2/3} g_3 g_4 / C.$$

– IF $\tilde{X}_c - 3\tilde{X}_n > 2 \rightarrow \omega_0 = \text{sign}(X_c)\omega_0^a, \dot{\varphi} = \text{sign}(X_n)\omega^a$

– ELSE $\omega_0 = \text{sign}(X_c)\omega_0^b, \dot{\varphi} = \text{sign}(X_n)\omega^b$

(f) Calculate \dot{c}_A, \dot{c}_I and $\dot{\varphi}$ (rate of change in orientation of normal) (if PT = 0 then $\dot{c}_A = 0, \dot{\mathbf{n}} = h_n \mathbf{X}_n$)

$$\dot{c}_A = 2\omega_0 R^2$$

$$\dot{c}_I = X_c^I$$

3. Calculate new values for $c_I, c_{II}, c_A, \mathbf{n}, \mathbf{n}_I$ using the simplest predictor–corrector method, $p = p + 1$

$$y_{n+1}^p = y_n + hf(y_n, t_n)$$

IF ($p = 1$) GOTO (2a)

ELSE $y_{n+1}^p = y_n + \frac{h}{2}[f(y_{n+1}^p, t_{n+1}) + f(y_n, t_n)]$

Replace y by $c_I, c_A, \varphi, \mathbf{n}_I$ (IF $PT = 0$, instead of φ use \mathbf{n})

IF ($c_A < 0$) THEN $c_A = 0.000001$

IF ($c_A > 1$) THEN $c_A = 0.999998$

IF ($c_I < 0$) THEN $c_I = 0.000001$

IF ($c_I > 1$) THEN $c_I = 0.999998$

Calculate c_{II} from $c_{II} = 1 - c_A - c_I$

$$c_{II} = 1 - c_A - c_I$$

$$n_1 = \cos \varphi, \quad n_2 = \sin \varphi$$

4. IF (kinetic loading) AND $PT = 1$ GOTO 2

ELSE check convergence for normal and volume fractions (stationary values).

IF $TOL > (\text{value})$ GOTO (2a)

– ELSE check phase transformation criteria

IF ($((\bar{X}_n - (1 - 0.25\bar{X}_c^2)) > 0)$ AND ($\tilde{X}_c > 0$)) THEN $PT = 1$ (start A–M transformation in the next step)

GOTO 2 (next load increment)

7. Examples

7.1. Effect of the athermal thresholds and loading paths

In this section, we will study the effect of the athermal thresholds for A–M and M_I – M_{II} interfaces and loading paths on stress–strain curves and transformations between A and M and between martensitic variants.

A number of uniaxial loading and unloading processes are studied under $\sigma_2 = \sigma_3 = 0$ with and without dissipation. The component ε_1 was varied from the initial value of -0.003 to 0.03 for the dissipation free case, and it was varied from some values between 0.03 and -0.003 to find the hysteresis loops for the case with dissipation. The stress σ , the dissipative threshold k , and the chemical part of the free energy $\Delta\psi^\theta$ are non-dimensionalized by $E\varepsilon_0$, where E is the Young's modulus and ε_0 is the maximum normal transformation strain. Thus, $\tilde{\sigma} = \sigma/(E\varepsilon_0)$, $\Delta\tilde{\psi}^\theta = \Delta\psi^\theta/(E\varepsilon_0)$, and $\tilde{k} = k/(E\varepsilon_0)$. We consider equal isotropic elastic properties of each variant and phases with equal Young's moduli and Poisson's ratio of $\nu = 0.3$. The transformational strains for cubic to tetragonal transformations, which are $\varepsilon_1^\dagger = 0.022$, $\varepsilon_2^\dagger = -0.011$, and $\varepsilon_3^\dagger = -0.011$ are used in the calculations. The difference in the chemical part of the free energy is taken as $\Delta\tilde{\psi}^\theta = 0.0034$. To model quasi-static deformation, we obtain the stationary solution for each strain increment.

Dissipative thresholds for the change of volume fractions for several different cases are investigated for loading and unloading. They characterize an athermal resistance to interface motion due to its interaction with crystal defects. The dissipative thresholds can be varied in a wide range by preliminary thermomechanical treatment. That is why we need to vary these thresholds in a wide range.

The variation of volume fractions of austenite and the martensitic variants, as well as stresses $\tilde{\sigma}_3$ in austenite, martensite, each martensitic variants and macroscopic stresses $\tilde{\sigma}_1$ are shown in Figs. 2a–f for the case when $\tilde{k} = \tilde{k}^I = 0.0034$. The case corresponding to $\tilde{k} = \tilde{k}^I = 0$ is designated with a dotted line HBCD (which coincides with the solution of Roytburd and Slutsker (2001)). All points correspond to the stationary solution for each prescribed ε_1 . The normal along the A–M interface is $\mathbf{n} = (0.7519, 0.6592, 0)$ and along M_I – M_{II} is $\mathbf{n} = (0.7071, 0, 0.7071)$. The effect of dissipative thresholds on the variation of c_A , c_I and c_{II} can be seen clearly. All the stresses $\tilde{\sigma}_2^A$, $\tilde{\sigma}_2^I$, $\tilde{\sigma}_2^{II}$ and all the internal stresses $\tilde{\sigma}_1$ and $\tilde{\sigma}_2$ are zero. The internal stresses $\tilde{\sigma}_3$ between austenite–martensite and variant–variant are significant. The process starts from point A and proceeds through the points EFD, while unloading goes through DFGHA. For unloading, there is no phase transformation up to a strain value of 0.02. Then, the transformation M_I – M_{II} starts and continues up to point G, where M–A transformation starts. If we interrupt the unloading process at point I and load again, we obtain the curve IJFD. The bold points represent the points where the unloading process is interrupted and the loading process starts, similarly. Between the points I and J, there is no transformation up to some point in the middle (this portion of the line is parallel to the lines HE and DC which are the corresponding loading lines of pure austenite and pure martensite) and then the transformation M_{II} – M_I starts and continues to point J. Then, the transformation A–M starts. At some point between JF, the second variant disappears (these points can be seen clearly in Fig. 2f) and the curve becomes a straight line. At point F, the phase transformation stops and we have elastic loading of the first martensitic variant. The internal stresses for A (or M) can be found by subtracting the macroscopic stress from the average stress in A (or M). The internal stresses appear only in the third cubic direction. For A (or M), the plot of the internal stresses is the same as in Fig. 2c (or Fig. 2b for M) because they are the difference between the average stress in A (or M) and macroscopic stress, where the total stress $\tilde{\sigma}_3$ is zero for the uniaxial case.

In Fig. 3a, the case $\tilde{k}^I = 0.0051$, $\tilde{k} = 0.0051$ is considered. The loading curve is ABC, the unloading curve is CDE, and an example of loading after the interruption of unloading is FGC. For loading, the second variant disappears at the point between B and G where the curve becomes a straight line. During unloading, between points D and F, first the M_I – M_{II} transformation occurs only up to point H and then the M–A transformation starts and stops at point I, where the strain is 0.005. Then the M_I – M_{II} transformation proceeds. Between F and G, there is no phase transformation up to point J, then the M_{II} – M_I transformation starts and then it stops slightly before point G is reached.

Figs. 3b–d show similar loading cases with different dissipative thresholds. When the threshold is smaller, as in Fig. 3b, the hysteresis is smaller as well. When $\tilde{k} = 0$, and $\tilde{k}^I \neq 0$, results coincide with the dissipation-free case at unloading and slightly deviate for loading. When there is a dissipation between A–M only, we obtain the curves in Fig. 3d. During the loading process ABC, the second variant disappears at some point between B and H. During unloading, the transformation of M_I – M_{II} first starts at point D and then the transformation of M–A starts at point I. However, after the beginning

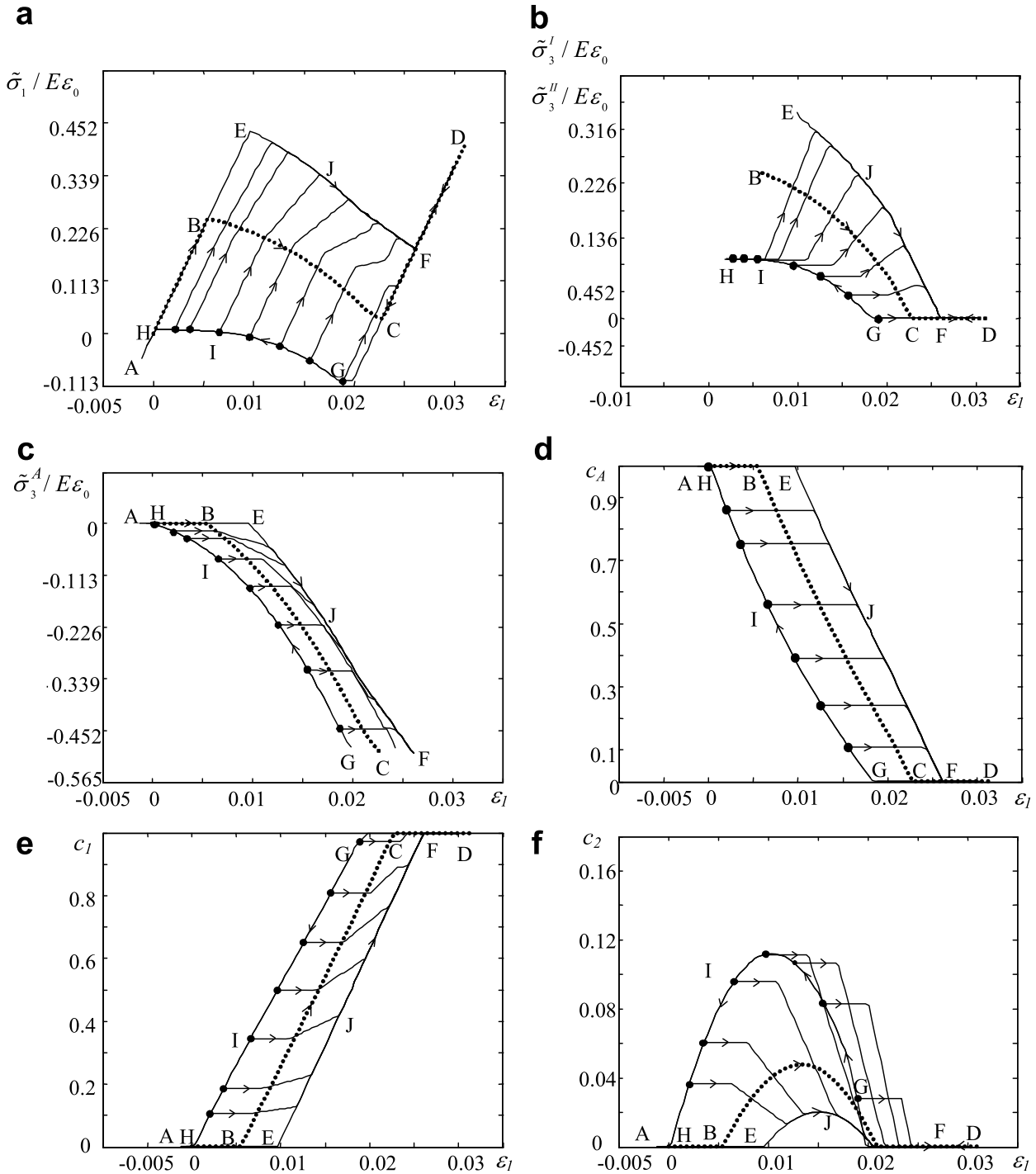


Fig. 2. Results of calculations for uniaxial stressing for $\tilde{k} = \tilde{k}^I = 0.0034$. Variation of (a) macroscopic stress $\tilde{\sigma}_1$, (b) stresses $\tilde{\sigma}_3$ in the martensitic variants, (c) stress $\tilde{\sigma}_3$ in austenite, (d) volume fraction of austenite c_A , (e) volume fraction of the first martensitic variant c_I and (f) volume fraction of the second martensitic variant c_{II} .

of the transformation, the stress remains constant at 0 until the end of the transformation. This occurs because of equal \tilde{k} and $\Delta\tilde{\psi}^\theta$ and because the dissipation-free transformation of M_I – M_{II} maintains the compatibility of the phases without internal stresses.

Fig. 4 represents the interruption of loading at some points and unloading from these points. For example, the loading ABCD is interrupted at point H and unloading continues to point F. There is no transformation on the line HE. Between E and F, we have the A–M

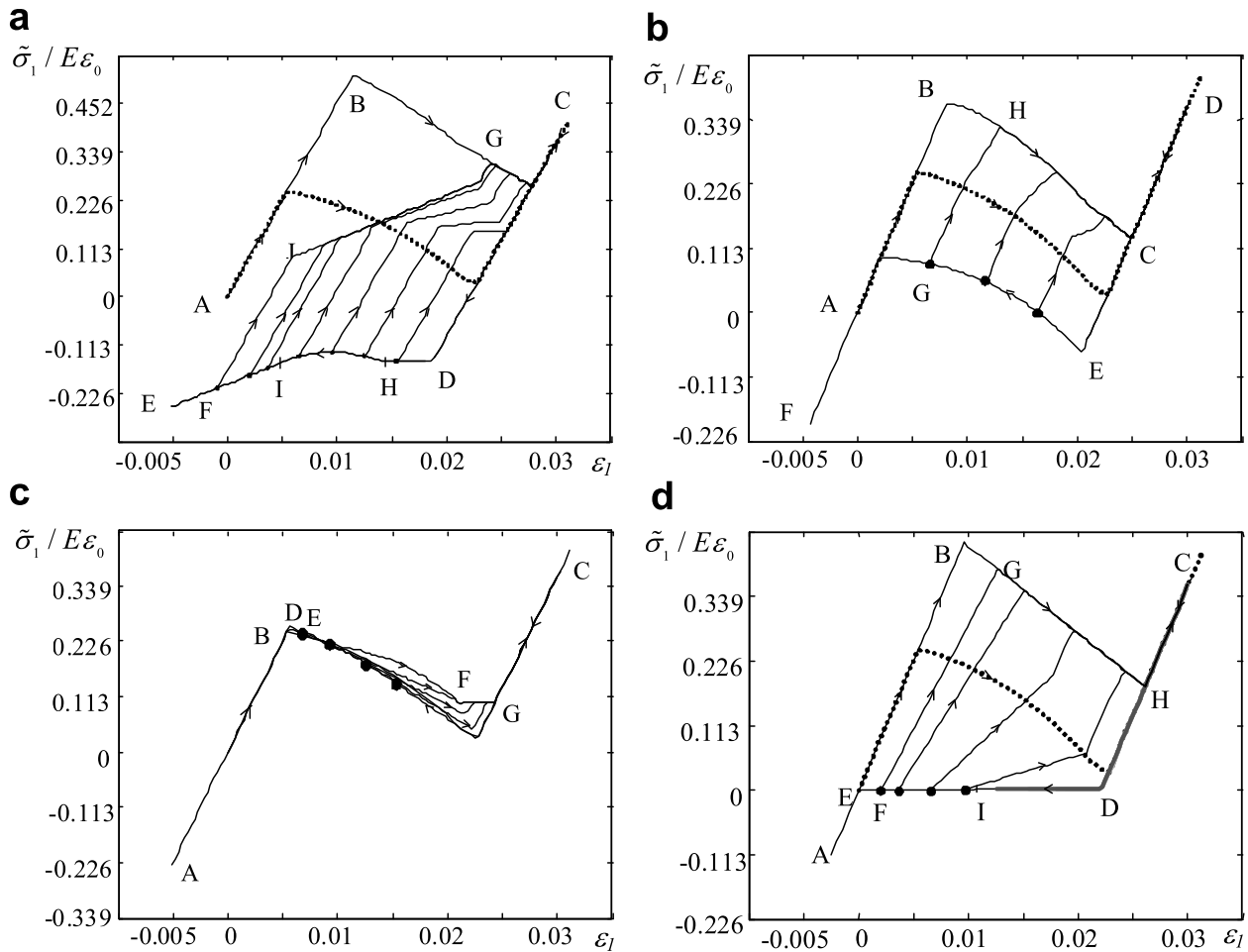


Fig. 3. Variation of uniaxial stress $\tilde{\sigma}_1$ for loading with (a) $\tilde{k} = \tilde{k}^I = 0.0051$, (b) $\tilde{k} = \tilde{k}^I = 0.0023$ and (c) $\tilde{k} = 0$, $\tilde{k}^I = 0.0034$ and (d) $\tilde{k} = 0.0034$ and $\tilde{k}^I = 0$.

transformation only for some strain values (around 0.005) and there is only the M_I – M_{II} transformation for the other points.

Figs. 5a–c represent multiple interruptions of loading and unloading processes for different values of thresholds. In Fig. 5a, the loading starts at point A and proceeds to B and C. Then the unloading is followed by the curve CDE and interrupted at E. Loading fol-

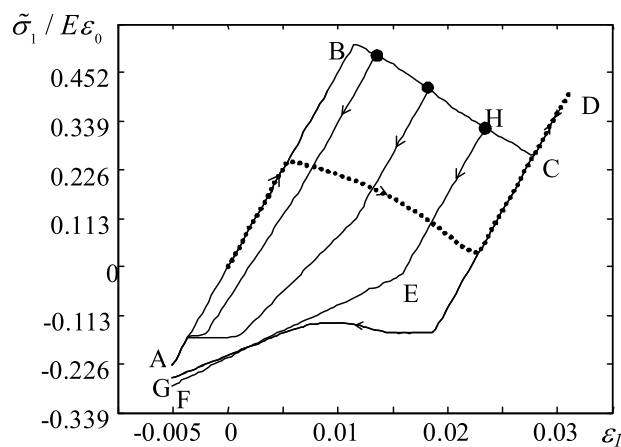


Fig. 4. Variation of uniaxial stress $\tilde{\sigma}_1$ for unloading with $\tilde{k} = \tilde{k}^I = 0.0051$.

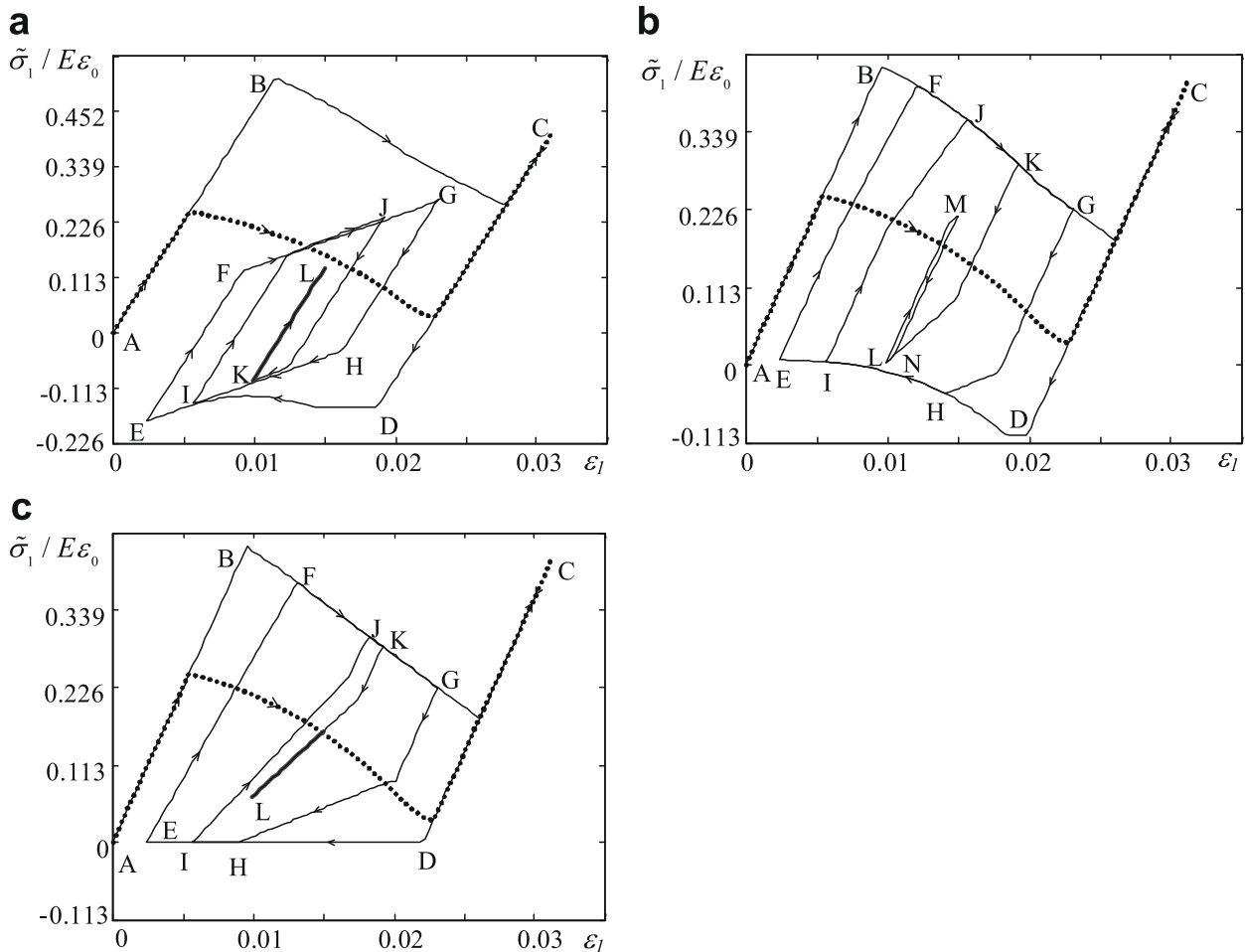


Fig. 5. Variation of uniaxial stress $\tilde{\sigma}_1$ for internal loading with (a) $\tilde{k} = \tilde{k}^I = 0.0051$, (b) $\tilde{k} = \tilde{k}^I = 0.0034$ and (c) $\tilde{k} = 0.0034$ and $\tilde{k}^I = 0$.

lows this process to point G, where loading is again interrupted to continue with unloading. So the total path starting from unloading point C is CDEFGHIJKL. There is no phase transformation for the lines parallel to EF, and there is only the M_I – M_{II} transformation for the lines FG and HE and for the lines parallel to them. Similar internal loops for the case of $\tilde{k}^I = 0.0034$ and $\tilde{k} = 0.0034$ are shown in Fig. 5b. The process is CDEFGHIJKLMN. For the case of $\tilde{k}^I = 0$ and $\tilde{k} = 0.0034$, the plot is shown in Fig. 5c. The path is CDEFGHIJKL, and if we start loading at L, it follows the same curve through K. The transformation characteristics are almost the same as those in the previous cases.

For modeling of biaxial loading, the material properties and the initial conditions are taken as the same as for the uniaxial model. A number of biaxial tension and compression processes are studied under $\tilde{\sigma}_2 = 0$. The component ϵ_3 was varied from the initial value 0.0 to 0.03 and from 0.0 to -0.03 for different fixed values of ϵ_1 to obtain tension and compression cases. The dissipative thresholds for volume fractions were taken as zero.

The phase transformation curve for the beginning of the phase transformation in the $\tilde{\sigma}_1$ – $\tilde{\sigma}_3$ plane for biaxial loading is given in Fig. 6. Inside the curve, the material behaves elastically without phase transformation. In the first quadrant the variants M_I and M_{III} appear; however, in the second quadrant only the third variant M_{III} appears on the upper line and only the second variant M_{II} appears on the lower line, in the third quadrant only the second variant M_{II} appears and in the fourth quadrant only the first variant M_I

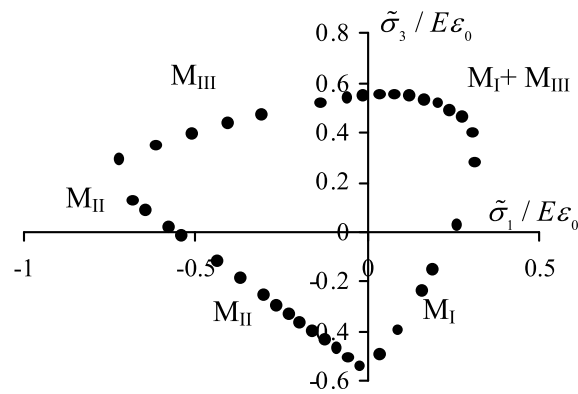


Fig. 6. Phase transformation curve for the beginning of phase transformation in the $\tilde{\sigma}_1$ – $\tilde{\sigma}_3$ plane for biaxial loading.

appears. That is why the curves in the second, third and fourth quadrants are straight lines.

To summarize, we found the following features of stress–strain curves for complex loading–unloading uniaxial straining:

- (a) For all cases with zero and non-zero athermal thresholds, the macroscopic stress $\tilde{\sigma}_1$ decreases with growing strain during the direct phase transformation. This decrease is caused by internal stresses. It will lead to material instability in the solution of a boundary-value problem for a finite sample which will result in localization of transformation strain and formation of the discrete martensitic microstructure (see Levitas et al., 2004; Idesman et al., 2005). Thus, these micromechanically-based constitutive equations can be used in the finite element method (FEM) simulation of the discrete multiconnected martensitic microstructure instead of pure phenomenological models in Levitas et al. (2004) and Idesman et al. (2005). It is known that the force–displacement (averaged stress–averaged strain) curve for a finite sample will be different from the local stress–strain curve in Figs. 2, 3 and 22 due to material instability and heterogeneous fields. Thus direct comparison of any unstable constitutive equations with a macroscopic experiment is not straightforward and requires special procedures.
- (b) The stress $\tilde{\sigma}_1$ during reverse phase transformation increases (in most cases) with decreasing strain, exhibiting similar material instability. However, in some cases, stress is zero (which still may lead to instability) or decrease near completing the reverse phase transformation. Such a stabilization is caused by martensite–martensite transformation and corresponding dissipation. The zero dissipation curve is the same for direct and reverse transformation.
- (c) Deviation of the stress–strain curve from the curve with zero dissipation is non-symmetric. For equal $\tilde{k} = \tilde{k}_I$, deviation for the reverse transformation is larger. For $\tilde{k} = 0$, there is small deviation for the direct transformation and no deviation for the reverse transformation. For $\tilde{k}_I = 0$, the deviation at the beginning of the reverse transformation is smaller than for the direct transformation but at the end it gets larger.
- (d) Behavior inside the hysteresis loop is very complex and accompanied by jumps in a slope of the stress–strain curve. This is a result of initiation and termination of M_I – M_{II} and A – M transformations. Even for monotonous increase (or decrease in strains), volume fraction of a martensitic variant can be non-monotonous (Fig. 2f).

7.2. Interface reorientation under complex loading

Two classes of numerical simulations were carried out to study the coupled evolution of the stresses and crystallographic parameters including the interface reorientation. In the first one, the tetragonal–orthorhombic phase transformations have been considered with $\boldsymbol{\varepsilon}^t = \{0.022; -0.011; -0.0044\}$ and $\tilde{k} = 0$ for quasi-static loading. The case with $k = 0$ allows us to treat three-dimensional interface reorientation.

In the second class, cubic–tetragonal phase transformations with $\boldsymbol{\varepsilon}^t = \{0.022; -0.011; -0.011\}$, $\Delta\tilde{\psi}^\theta = 0.0045$ (unless other values are given) and $\tilde{k} > 0$ for $\dot{\varepsilon}_1 = 0.0025 \text{ s}^{-1}$ and also for quasi-static loading have been studied. Here two-dimensional interface evolution was analyzed. The following material properties were used in all calculations: the Young's moduli $E_M = 4E_A$ or (when specifically stated) $E_A = 3E_M$, the Poisson's ratio, $\nu_A = \nu_M = 0.3$; and the coefficient of viscosity $\lambda = 0.00136 \text{ s/m}$. The variables designated with a \sim are non-dimensionalized by $E_M \varepsilon_0$.

The interface between martensitic variants does not rotate because of equal elastic moduli. The interface length $2R$ was determined from the geometry for the unit cube. When two martensitic variants have been allowed, we used $\tilde{k}^1 = 0$. For each simulation, an embryo with $c_M = 10^{-4}$ was introduced by locating the planar interface Σ very near a corner of the cube. The initial interface orientation, \mathbf{n}_0 , was either determined from the condition $\mathbf{X}_n = 0$, which gives the “optimal” (energy minimizing) orientation, or assigned a non-optimal value. The non-optimal \mathbf{n}_0 mimics the presence of a stress field of various defects (dislocations, grain and twin boundary, etc.) (Levitas and Ozsoy, 2008). One of our goals was to find loading programs that exhibited non-trivial interface behavior, including large interface reorientation and orientational instability.

7.2.1. Three-dimensional interface reorientation for tetragonal to orthorhombic phase transformation with $\tilde{k} = 0$

The following examples have been considered.

1. The tetragonal–orthorhombic phase transformation was studied for prescribed strains corresponding to the uniaxial tensile stress $\tilde{\sigma}_3$ ($\tilde{\sigma}_1 = \tilde{\sigma}_2 = 0$). To study interface reorientation without propagation, the value $c_A = 0.7014$ was held constant by changing the temperature, or more exactly $\Delta\tilde{\psi}^\theta$. The jump in thermal energy, $\Delta\tilde{\psi}^\theta$, was determined from the condition $X_c = 0$. The initial equilibrium interface normal corresponding to $\mathbf{X}_n = 0$ was $\mathbf{n}_1 = (a, b, 0)$, where $a = 0.79$ and $b = 0.61$. Due to symmetry there are three crystallographically, but not energetically, equivalent normals \mathbf{n}_i obtained by cyclic permutation of the components of \mathbf{n}_1 . The Gibbs energy has a multiwell structure as a function of the \mathbf{n}_j : the local minima are located at the \mathbf{n}_i and are separated by potential barriers. For the applied tensile stress $\tilde{\sigma}_3$ the Gibbs energy is minimized for the normal $\mathbf{n}_2 = (a, 0, b)$. However, during loading up to $\varepsilon_3 < 0.004$, the normal does not vary (Fig. 7) because the local metastable energy minimum at \mathbf{n}_1 is separated from the stable energy minimum at \mathbf{n}_2 by a finite potential barrier. At $\varepsilon_3 = 0.004$ the minimum at \mathbf{n}_1 and the potential barrier disappear, hence an abrupt interface rotation occurs toward the stable normal \mathbf{n}_2 . The interface rotation is accompanied by jumps in stress $\tilde{\sigma}_3$ and $\Delta\tilde{\psi}^\theta$. Further loading does not induce additional interface rotation. Thus, we find that an instability in the interface normal leads to a jump-like interface reorientation that has the following features of

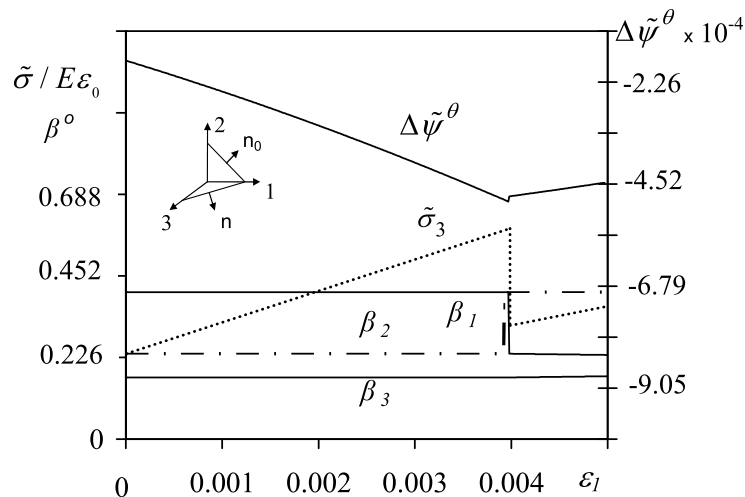


Fig. 7. The change in the three direction angles β_i for the normal \mathbf{n} for the applied uniaxial stress $\tilde{\sigma}_3$ and temperature variation $\Delta\tilde{\psi}^\theta$.

the energetics of a first-order phase transformation: there are multiple energy minima that are separated by an energy barrier; positions of minima do not change in the \mathbf{n}_i space during loading but their depth varies; when the barrier disappears (i.e. one of the minima transforms to the local saddle or maximum points), the system rapidly evolves toward another stable state.

- For the complex multi-axial straining shown in Fig. 8a, results of variation in the volume fraction of austenite and three direction angles for the normal \mathbf{n} are shown in Fig. 8b. Temperature was held constant. Initially, there is a very small change in β_1 and β_2 during direct transformation. Adding compressive ε_2 component does not change the rate of the phase transformation and stabilizes the interface orientation. Significant change in a loading path at $t = 1000$ s causes the reverse transformation but does not change the interface normal. Finally, reduction in compressive strain ε_2 intensifies the reverse phase transformation until its completion. It also causes a large stable variation in interface normal orientation (Fig. 8b); in particular, angle β_3 changes by 27° .

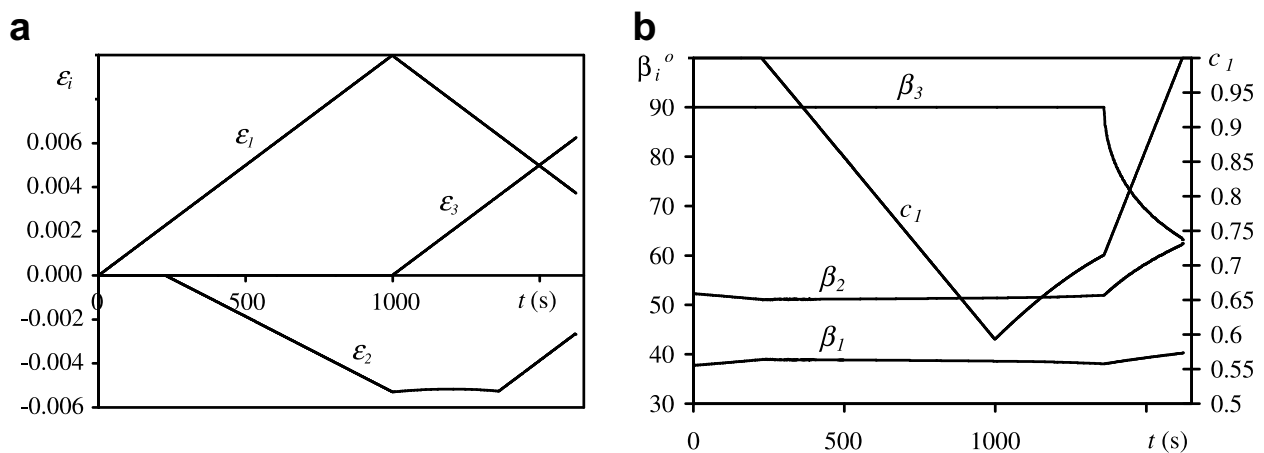


Fig. 8. (a) Prescribed strain history and (b) variation of volume fraction of austenite c_1 and three direction angles for the normal \mathbf{n} .

3. For the complex multi-axial straining shown in Fig. 9a, the problem is solved for one and two martensitic variants. The variation of the macroscopic stresses are presented in Fig. 9b and the evolution of volume fractions of the austenite and martensitic variants, as well as direction angles for the normal are shown in Fig. 9c. The difference between one and two martensitic variants is drastic. For one variant, direct transformation is followed by the reverse transformation that completes at $t = 1320$ s; there are no changes under further loading. For two martensitic variants, reverse transition is very modest and then it turns to the direct phase transformation again. Changes occur during the entire loading until $t = 2500$ s and the final state is a mixture of the austenite and the variant M_{II} . When there is only one martensitic variant, the jump in the interface normal is from the 1–2 plane to the 1–3 plane, while it is from the 1–2 plane to the 2–3 plane when two variants of martensite are present. In both cases, the jump in the normal is accompanied by a jump in volume fractions and all macroscopic stresses. For the two-variant case, the first variant of martensite suddenly disappears which is caused by a jump in the orientation. The phase transformation proceeds between austenite and second variant of martensite after this point. Note that if no perturbations are applied during the computations, the unstable path shown after $t = 2250$ s is obtained which corresponds to a saddle point of the energy.

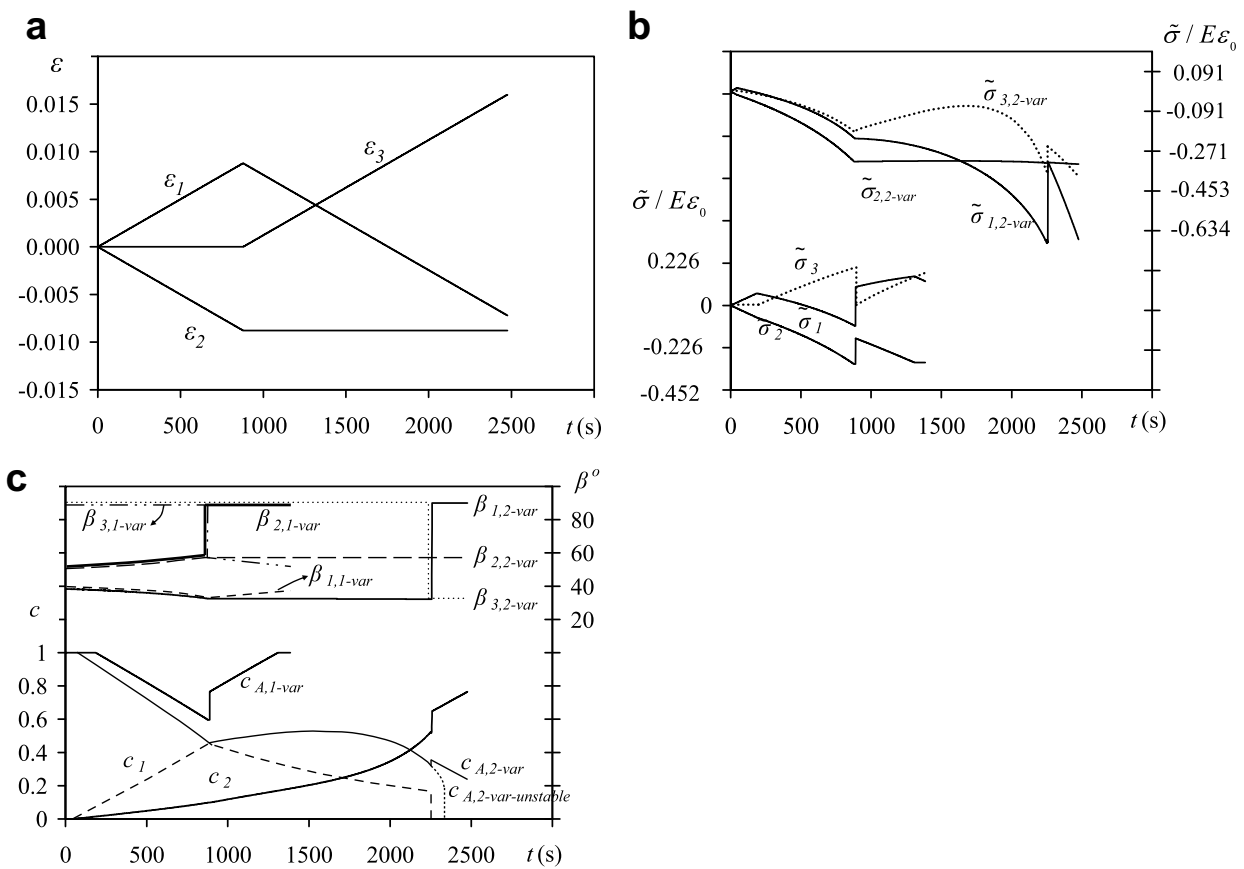


Fig. 9. (a) The loading path, (b) variation of stresses $\tilde{\sigma}_1$, $\tilde{\sigma}_2$ and $\tilde{\sigma}_3$, (c) variation of volume fractions c_A , c_1 , c_{II} and the orientations β with respect to three cubic axes for the case with one and two martensitic variants.

4. Fig. 10 contains results for $\Delta\tilde{\psi}^\theta = 0.0045$ and the following straining $\varepsilon_2 = -\varepsilon_1$ and $\varepsilon_3 = 0$, i.e. for pure shear between rigid walls. When only one variant of martensite exists, the phase transformation starts at $\varepsilon_1 = 0.0051$. When the volume fraction of martensite reaches 0.55 (at $\varepsilon_1 = 0.0128$), a jump in the orientation occurs and it is accompanied by a jump in stresses and a small jump in volume fraction. While the normal was in the 1–2 plane before the jump, it is in the 1–3 plane after, and the phase transformation proceeds without further interface rotation until austenite completely transforms to martensite. For two martensitic variants, the phase transformation starts earlier since the addition of the second variant minimizes the energy of internal elastic stresses. Phase transformation starts at $\varepsilon_1 = 0.0042$, and austenite transforms to martensite completely without a jump in volume fraction and orientation of the interface. The direction angle in the 1–2 plane varies from $\beta_1 = 38.4^\circ$ to 36.4° inside the embryo and then to 6° during phase transformation.
5. For the same straining but $\Delta\tilde{\psi}^\theta = 0.00045$, variations in volume fractions c_A , c_I , c_{II} and the direction angle in the 1–2 plane β are shown in Fig. 10c. The continuous change in orientation is greater (about 23°) when there is only one variant of martensite. For two martensitic variants the change in orientation is about 18° .

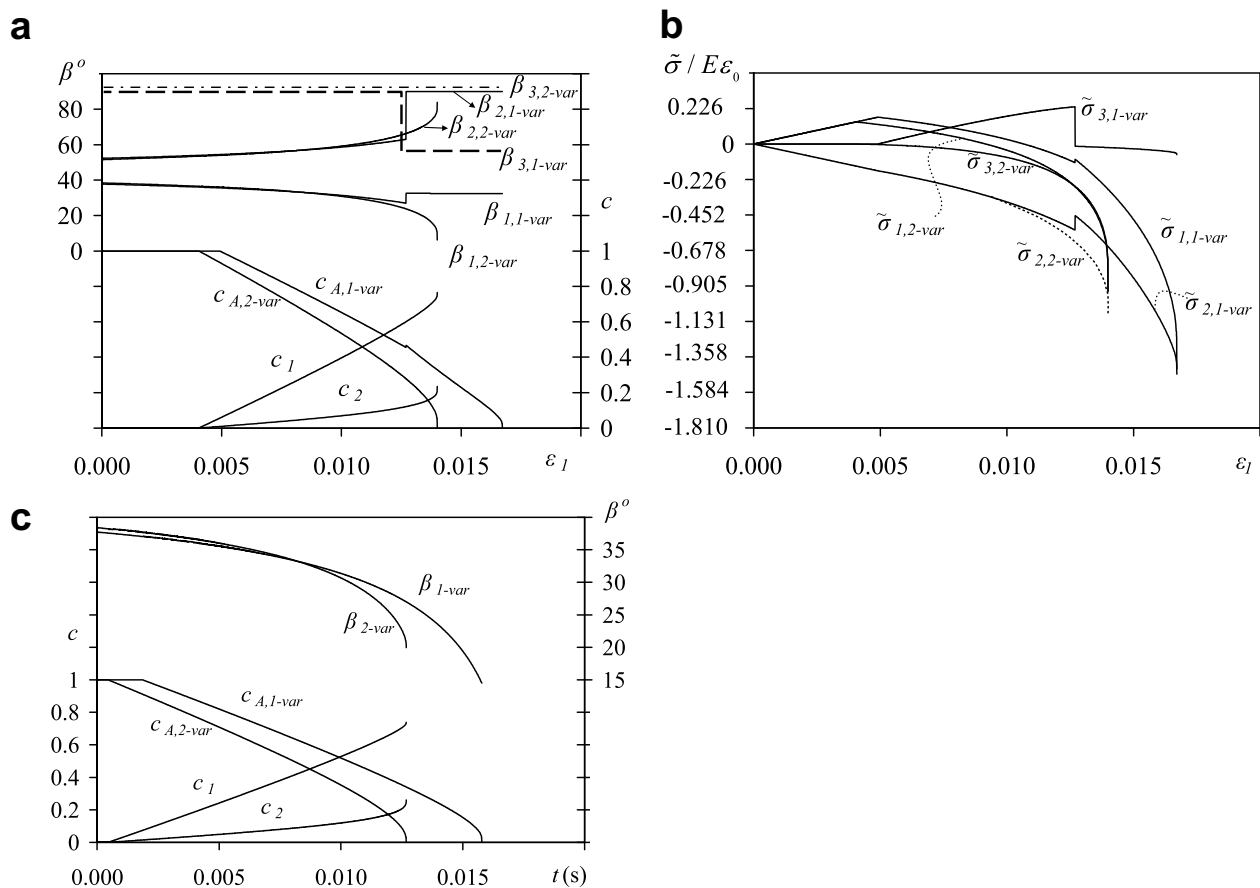


Fig. 10. For the loading $\varepsilon_2 = -\varepsilon_1$ and $\varepsilon_3 = 0$ and $\Delta\tilde{\psi}^\theta = 0.0045$, (a) the change in volume fractions and the A–M orientation for phase transformation with one and two martensitic variants, (b) variations in stresses $\tilde{\sigma}_1$, $\tilde{\sigma}_2$ and $\tilde{\sigma}_3$ and (c) variations of volume fractions c_A , c_I , c_{II} and the orientation β for the same loading but with $\Delta\tilde{\psi}^\theta = 0.00045$.

6. Fig. 11 shows the result for two martensitic variants under the growing compressive strain ε_2 at $\varepsilon_1 = \varepsilon_3 = 0$ (straining similar to the shock wave) with $\Delta\tilde{\psi}^\theta = 0.0023$. After phase transformation starts, continuous interface rotation takes place, and at the end, instabilities in volume fractions and interface orientation occur. The variation in the interface orientation is from $\beta = 38.3^\circ$ to 30.8° in the embryo and to 2° after the complete phase transformation. For all examples in this subsection below, $\Delta\tilde{\psi}^\theta = 0.00045$.
7. For the uniaxial tension and unloading shown in Fig. 12a, results are qualitatively similar for single and two variant cases. For two variants, the transformation starts earlier and the change in orientation is higher (Fig. 12b). Note that due to lateral constrains, all stresses grow during the direct transformation and reduce during the reverse transformation, i.e. there is no material instability during the phase transformation. Also, since $\tilde{k} = 0$, there is no stress hysteresis, i.e. region without the transformation when unloading starts. The interface normal lies in the 1–2 plane.

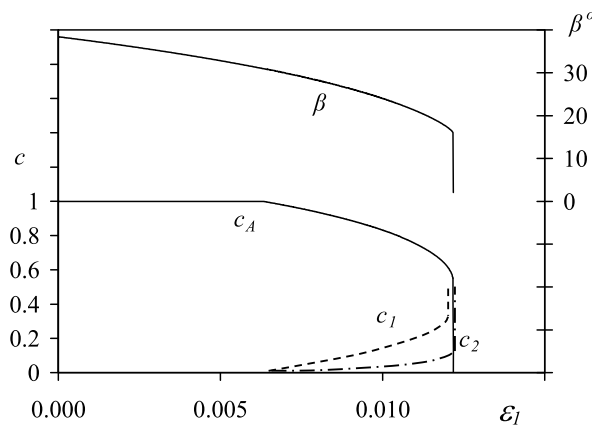


Fig. 11. Variation of volume fractions c_A , c_I , c_{II} and the orientation β for the transformation of austenite to two martensitic variants.

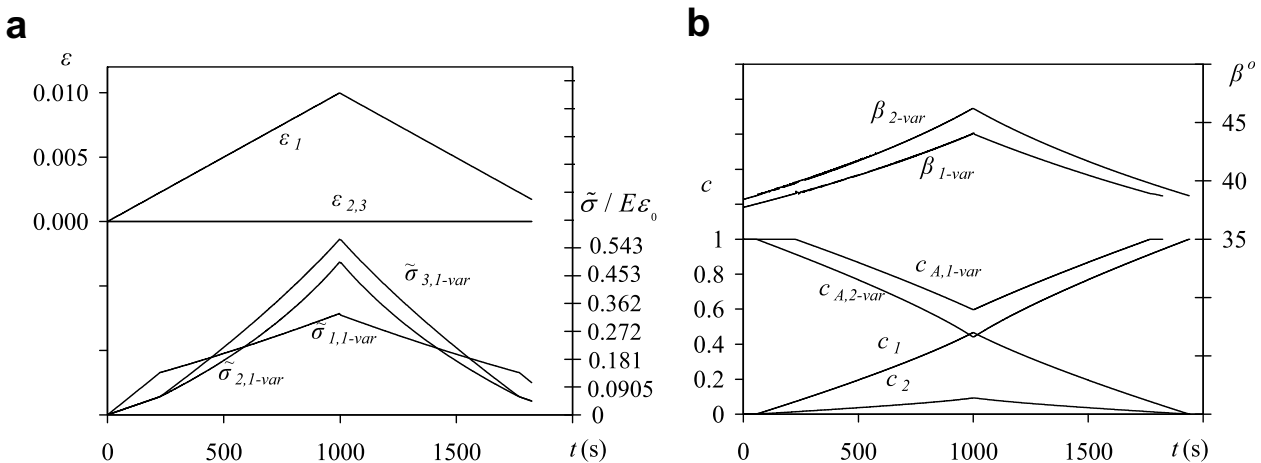


Fig. 12. (a) Uniaxial straining and macroscopic stresses when there are two variants of martensite and (b) the change in volume fractions c_A , c_I , c_{II} and orientations β for one and two variant cases.

8. The difference between Figs. 13 and 12 is the addition of strain in direction 3 during unloading in direction 1. If only one martensitic variant is present, the complete transformation of martensite to austenite occurs at the end of the specified loading along with instability in both volume fractions and orientation. The orientation changes its plane at the end of loading. However, when there are two martensitic variants, austenite transforms to martensite completely with continuous interface rotation and the plane containing the normal does not change. For the same loading but with $E_A/E_M = 3$ and two martensitic variants, the direct transformation follows by reverse transformation (Fig. 13c). There is 10.5° change in the orientation β during the transformation without any instability as opposed to the case in Fig. 13b. When single martensitic variant is allowed only, the results do not change much, because the concentration of the second variant is very low in the former example.
9. The prescribed straining in Fig. 14 consists of tension along direction 1 and equal compression in two other directions. The change in the interface orientation within the 1–2 plane is larger for a single martensitic variant. This is due to the larger strains necessary to complete the phase transformation. At the end of transformation, there is a jump in the volume fraction without a change in the interface orientation. The jump in orientation is accompanied by a jump in volume fractions when two

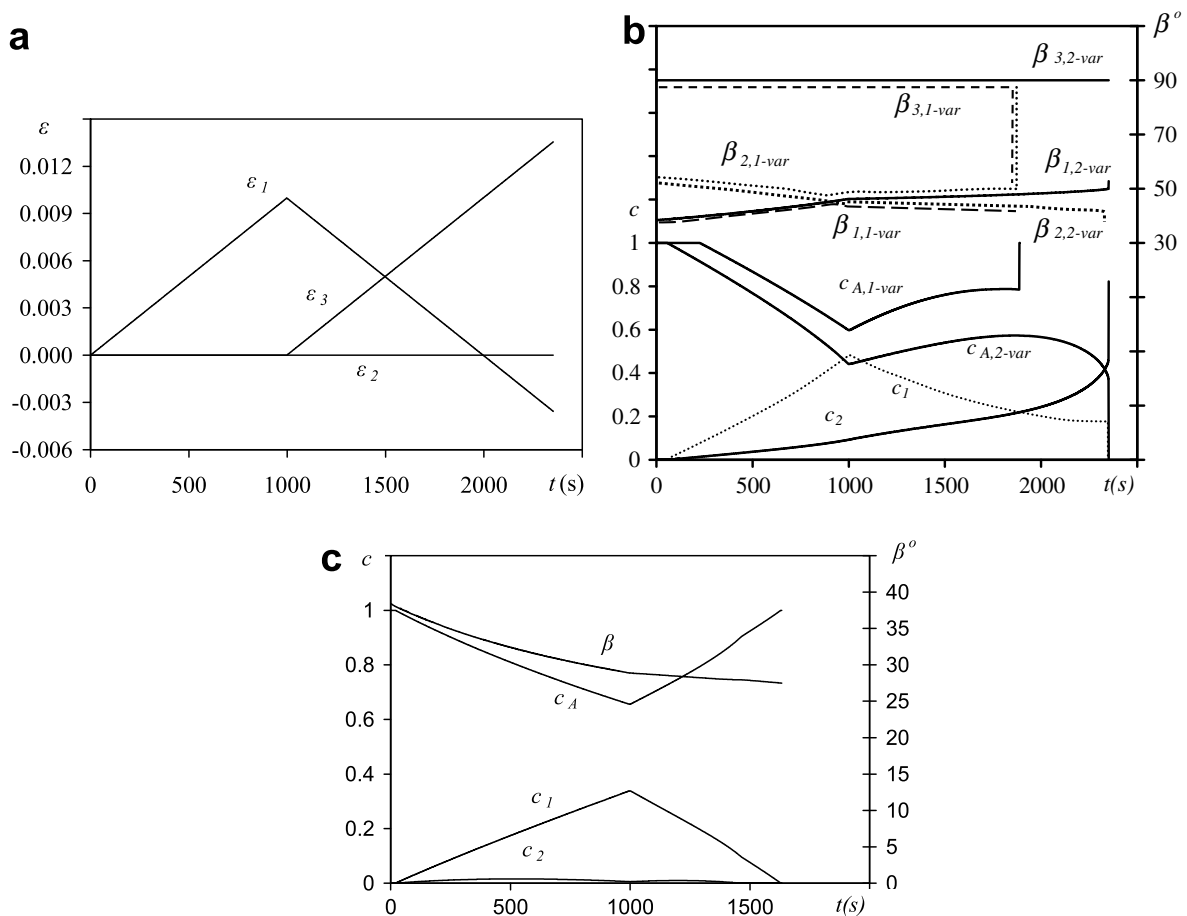


Fig. 13. (a) Prescribed strain history and (b) variations in volume fractions c_A , c_I , c_{II} and orientations β for $E_M/E_A = 4$; (c) the same for $E_M/E_A = 3$.

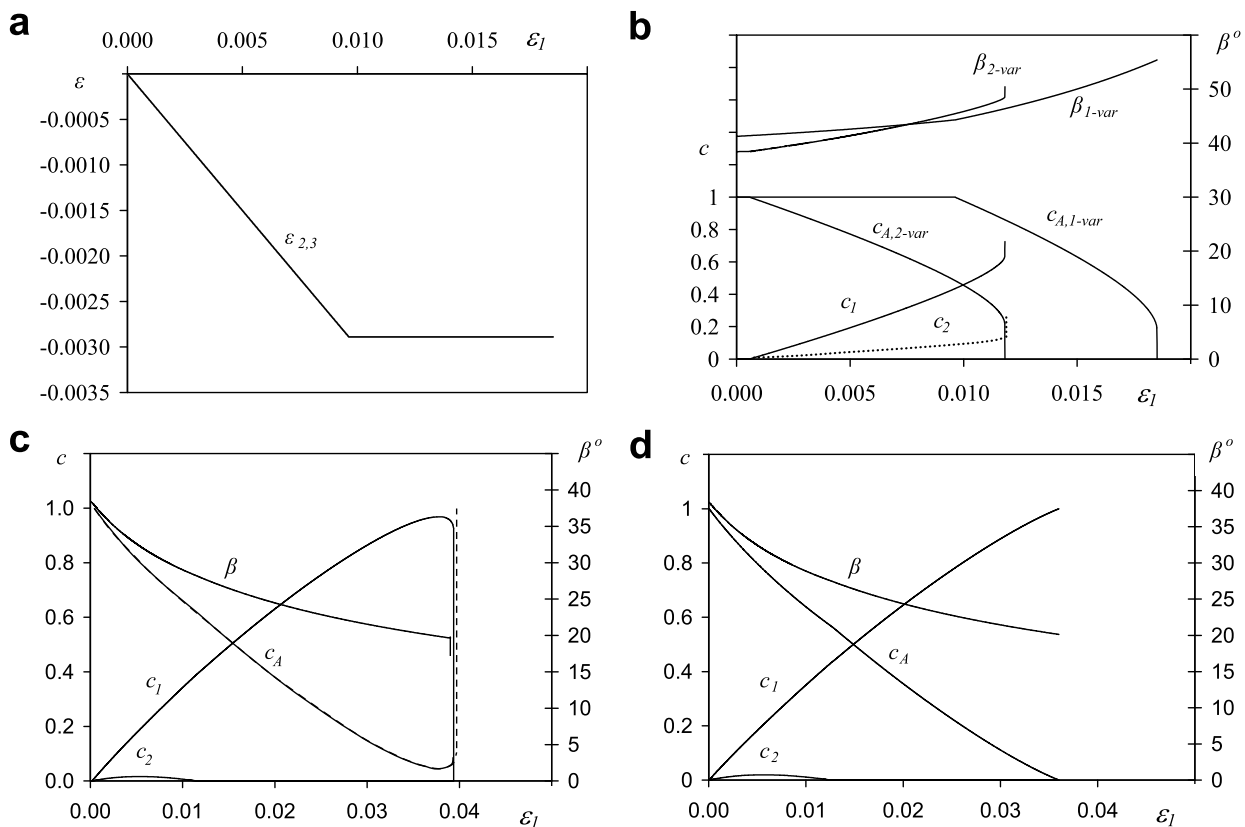


Fig. 14. (a) Prescribed strain history and (b) variations in volume fractions c_A , c_I , c_{II} and orientations β for one and two variant cases for $E_M/E_A = 4$; (c) variations in volume fractions c_A , c_I , c_{II} and orientation β for two-variant case when $E_A/E_M = 3$ and $\Delta\tilde{\psi}^\theta = 0.00045$; (d) same as (c) but with $\Delta\tilde{\psi}^\theta = 0.00009$.

martensitic variants are present. The orientation of the interface varies from $\beta = 41.3^\circ$ to 44.5° inside the embryo and to 55.4° at the end of transformation for one martensitic variant. On the other hand, it does not vary much inside the embryo when two martensitic variants exist and varies from $\beta = 38.5^\circ$ to 50.4° during continuous phase transformation. For $E_A/E_M = 3$ and the same loading, the result are shown in Fig. 14c. Just before completing the direct phase transformation, the jump-like complete reverse transformation occurs which is accompanied by a jump in normal. This jump is similar to that in volume fraction of austenite in Fig. 14b, but in opposite direction. This change is related to change in sign in jump in elastic strain. The angle β changes significantly from 38.2° to 19.6° during direct transformation. The second martensitic variant first appears in a very small amount with the start of phase transformation, but at $t = 1150$ s it disappears. Therefore, the behavior of the single variant system, which is not shown, is almost the same. When the temperature for the same loading is decreased to $\Delta\tilde{\psi}^\theta = 0.00009$ (Fig. 14d), the complete transformation of $A \rightarrow M$ occurs before the instability seen in Fig. 14c takes place. There is also a large continuous change in the angle β from 38.4° to 20.1° .

- For the straining shown in Fig. 15, the change in interface orientation for one martensitic variant is smaller than that for two variants. Thus, the change in normal can be either larger or smaller for a different number of variants (one or two) depending on the prescribed loading history. For both cases, after the change in loading, reverse

transformation occurs for a while, and then again direct transformation starts. At the completion of martensitic transformation, a large jump in volume fraction occurs for both cases. However, for two variants only, there is a small jump in orientation.

11. For the straining shown in Fig. 16a, the results in Fig. 16b look very similar to those in Fig. 14, despite the different straining. The direction angle for the normal for one martensitic variant is larger than for two martensitic variants for all strains but this is not the case at the end of the transformation (in contrast to Fig. 14).
12. For pure shear with no strain in the orthogonal direction shown in Fig. 17, when the loading is interrupted before completing the transformation and the material is unloaded as shown, reverse transformation follows the same path due to the absence of dissipation. Since the transformation for two variants starts earlier than for one variant, the change in orientation is larger for two martensitic variants (about 15°). This change is about 10° for one martensitic variant.

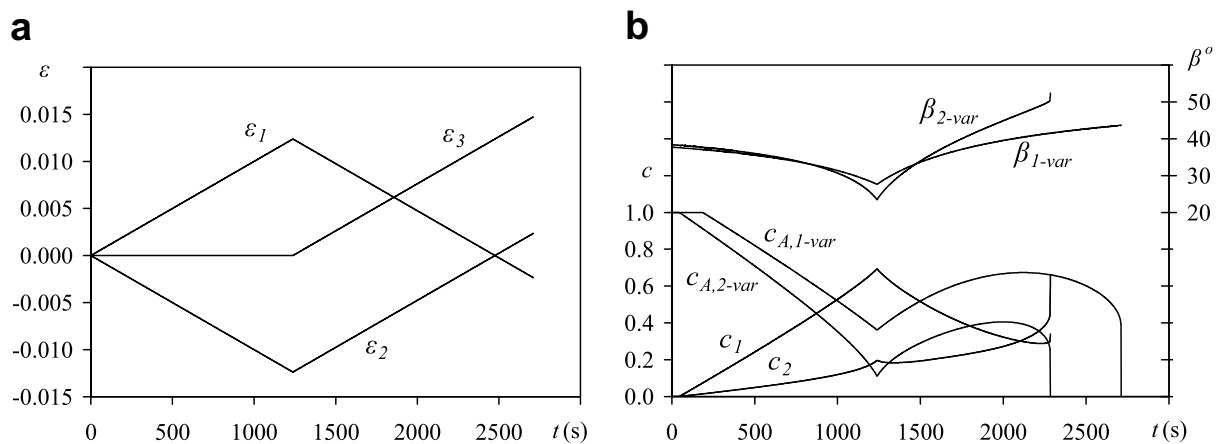


Fig. 15. (a) Prescribed strain history and (b) the change in volume fractions c_A , c_I , c_{II} and orientations β for one and two variants.

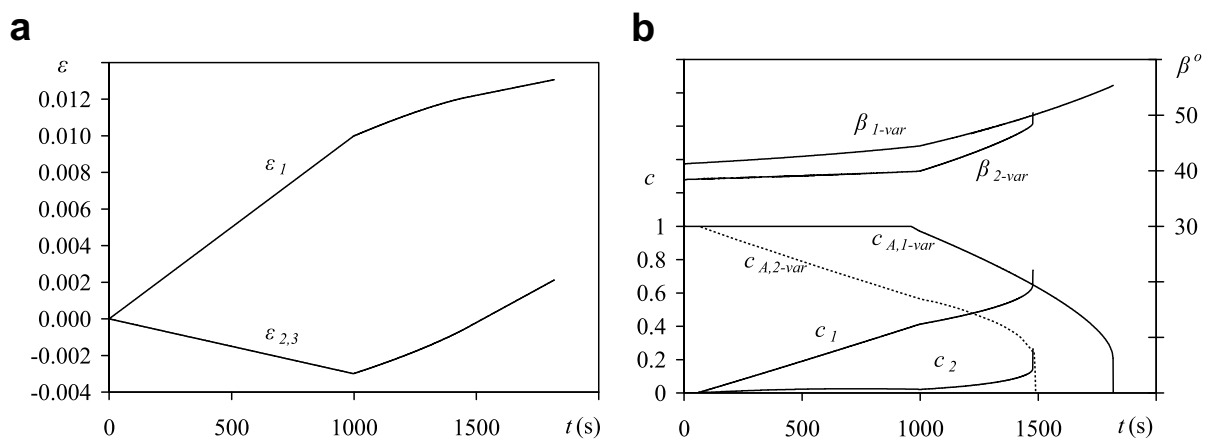


Fig. 16. (a) The loading path (pure shear with no strain in the orthogonal direction) and (b) the change in volume fractions c_A , c_I , c_{II} and orientations β for one and two variant cases.

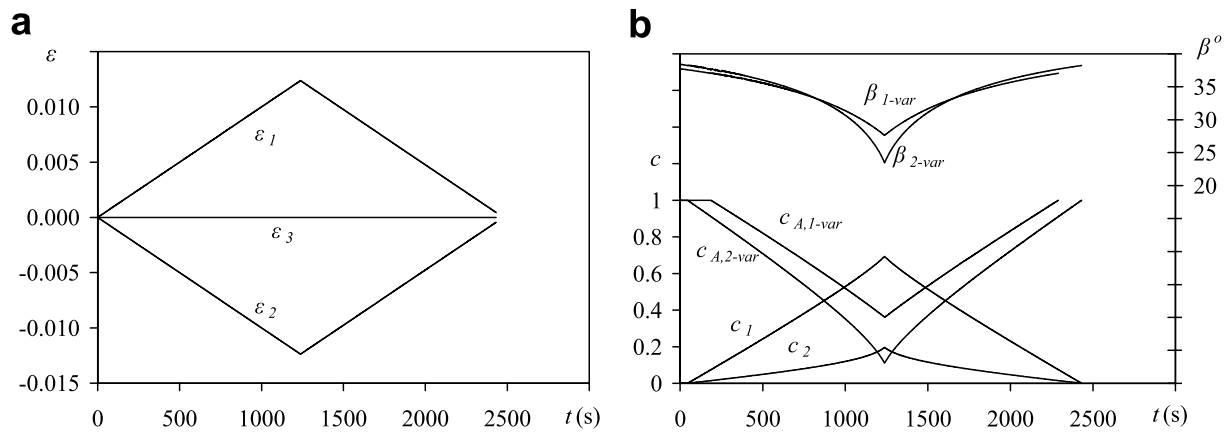


Fig. 17. (a) Prescribed strain history and (b) the change in volume fractions c_A , c_I , c_{II} and orientation β .

7.2.2. Three-dimensional interface reorientation for cubic to tetragonal phase transformation with $\tilde{k} = 0$

Two examples have been considered with $E_A/E_M = 3$ (like for NiTi) and $E_M/E_A = 4$.

1. The loading for the results shown in Fig. 18a is $\epsilon_2 = -0.3\epsilon_1$ and $\epsilon_3 = 0$ for $E_A/E_M = 3$. There is a continuous transformation between austenite and martensitic variants. The angle β is 44.2° at the beginning and it goes down to 32.6° during the transformation. The interface reorientation occurs within a plane. The results for the same loading for $E_M/E_A = 4$ are shown in Fig. 18b. At the end of the transformation, a jump in the orientation occurs due to a jump in the volume fractions. The change in the angle β is about 13° during such a loading including the change in embryo.
2. For the prescribed complex loading in Fig. 19a, the change in volume fraction of austenite c_A and the variation in the three direction angles β_1 , β_2 and β_3 are shown in Fig. 19b for $E_A/E_M = 3$. Before the addition of the strain ϵ_2 , the change in angle β_1 is about 9° including the change in an embryo. The energy depends on β_1 up to this point only, i.e. β_2 and β_3 are arbitrary. After adding the strain ϵ_2 , the shown solution

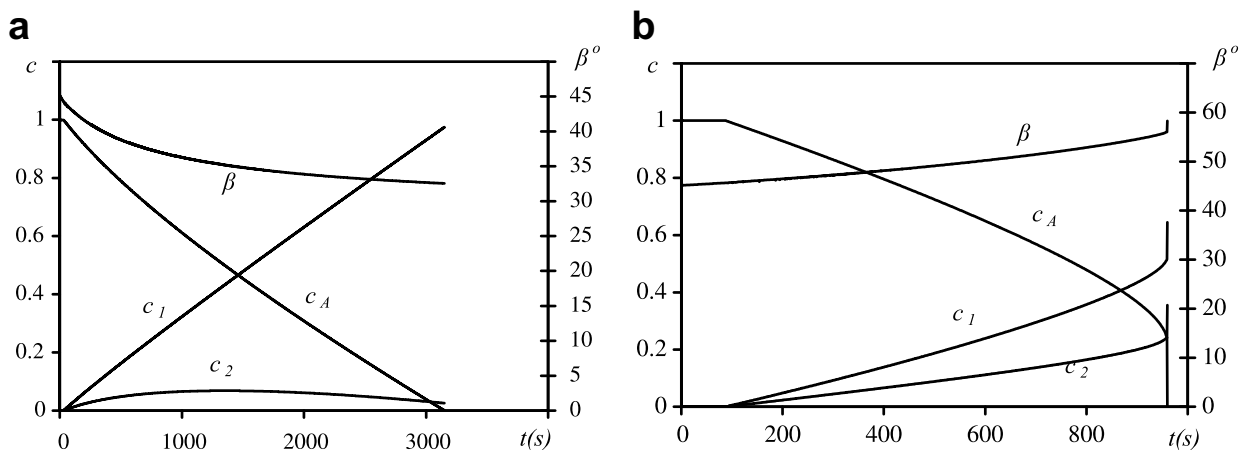


Fig. 18. Variation of the volume fractions c_A , c_I and c_{II} and the variation in the direction angle β for the loading $\epsilon_2 = -0.3\epsilon_1$ and $\epsilon_3 = 0$ (a) for $E_A/E_M = 3$ and (b) for $E_M/E_A = 4$.

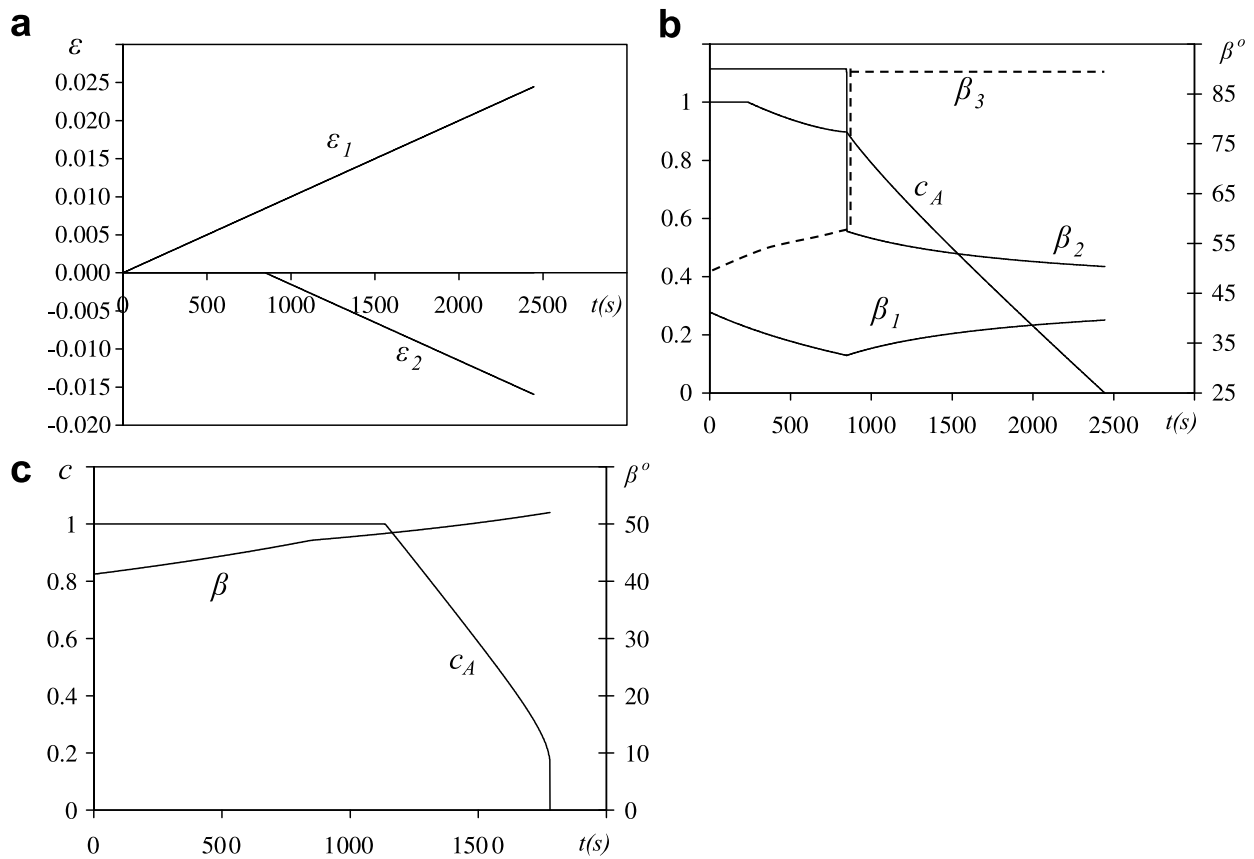


Fig. 19. Prescribed strain history (a), variation of the volume fraction c_A and the variation in the direction angles β_1 , β_2 and β_3 (b) for $E_A/E_M = 3$ and (c) for $E_M/E_A = 4$.

is the only one which corresponds to the minimum of the energy. Independent of the initial β_2 and β_3 , the solutions converge to the one shown in Fig. 19b. For the same loading and $E_M/E_A = 4$, the results are presented in Fig. 19c. Interface orientation continuously evolves within single plane. The phase transformation start point is significantly delayed and the change in angle β inside the embryo is about 7° , while it is about 4° during the transformation.

7.2.3. Two-dimensional interface reorientation for cubic to tetragonal phase transformation with $\tilde{k} > 0$

The following examples have been considered.

1. In the example in Fig. 20, the straining represents pure shear $\varepsilon_2 = -\varepsilon_1$ and $\varepsilon_3 = 0$. For a single martensitic variant and $\tilde{k} = 0$, the transformation starts at $\varepsilon = 0.0087$ and proceeds with a continuous interface rotation, where direction angle β_1 varies by 2° only inside the embryo and by the same amount during the phase transformation (the subscript designates different cases in Fig. 20). The interface lies in the 1–3 plane for this case. When the second variant is added with $\tilde{k} = 0$, the phase transformation starts and ends early (because of the possibility of the additional energy minimization) with almost no change in the interface orientation during the loading. However, when $\tilde{k} > 0$, surprisingly large reorientation is observed. For example,

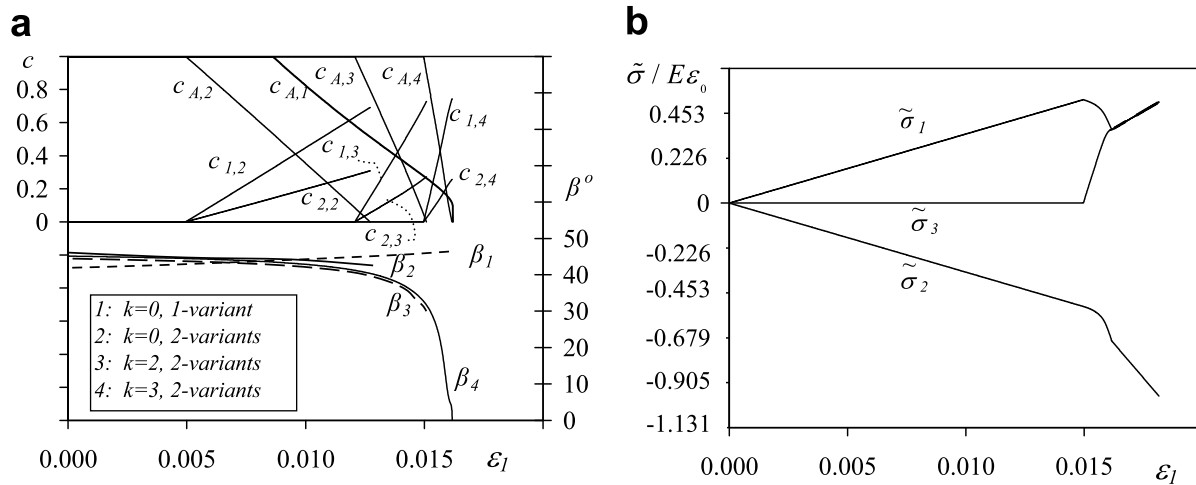


Fig. 20. For the loading $\epsilon_2 = -\epsilon_1$ and $\epsilon_3 = 0$ and $\tilde{k} = 0.0136$, (a) variations in volume fractions c_A, c_I, c_{II} and orientations β_i and (b) average stresses $\tilde{\sigma}_1, \tilde{\sigma}_2$ and $\tilde{\sigma}_3$.

when $\tilde{k} = 0.0136$, phase transformation starts at $\epsilon = 0.015$ and the interface orientation varies continuously from $\beta_4 = 45.1^\circ$ to $\beta_4 = 32.7^\circ$ inside the nucleus and to $\beta_1 = 0^\circ$ during phase transformation. Different from the single variant case, the interface lies in the 1–2 plane. As a demonstration, the macroscopic stress variation for $\tilde{k} = 0.0136$ and two martensitic variants are shown in Fig. 20b. The behavior is the same for all \tilde{k} values. When transformation starts, the reduction in $\tilde{\sigma}_1$ (an expected instability) is accompanied by growth in tensile stress $\tilde{\sigma}_3$ and compressive stress $\tilde{\sigma}_2$. In martensitic variants, the stresses $\tilde{\sigma}_1^M$ and $\tilde{\sigma}_3^M$ are equal to each other all the time (during and after the phase transformation). Hence, after completing the transformation, the macroscopic stresses are $\tilde{\sigma}_1 = \tilde{\sigma}_3$.

2. For the tensile uniaxial straining ϵ_1 with $\epsilon_2 = \epsilon_3 = 0$, the change in the orientation is about 13° when two variants of martensite are present (Fig. 21a). A jump in the volume fractions occurs at the end of the transformation which results in a jump in the orientation. Remarkably, there is not any stress relaxation due to phase transformation; a jump-like increase in the volume fraction of martensite is accompanied by a jump-like increase in all of the stresses. This happens because an increase in elastic strain due to an increase in Young's modulus exceeds the relaxation of elastic strains due to transformation strain. For $E_A/E_M = 3$, a small amount of austenite transforms initially to martensite, then a jump-like complete reverse transformation occurs with jump in normal (Fig. 21c). Large change in the angle β is observed. Stresses grow during the reverse transformation (Fig. 21d), because again an increase in elastic strain due to an increase in Young's modulus exceeds the relaxation of elastic strains due to disappearance of transformation strain.
3. For the loading like in a shock wave (compressive ϵ_2 with $\epsilon_1 = \epsilon_3 = 0$), the change in orientation is greater when two martensitic variants are present (Fig. 22). Interfaces belong to different planes for one and two variants. For a single variant and $\tilde{k} = 0$, the phase transformation starts at a larger strain than for two variants and $\tilde{k} = 0.0045$. The change in orientation of the interface increases with an increase in \tilde{k} . At the end of the loading, a jump in volume fractions occurs for all cases. For two variants and $\tilde{k} = 0.0045$, it is accompanied by a jump in the normal. Orientation

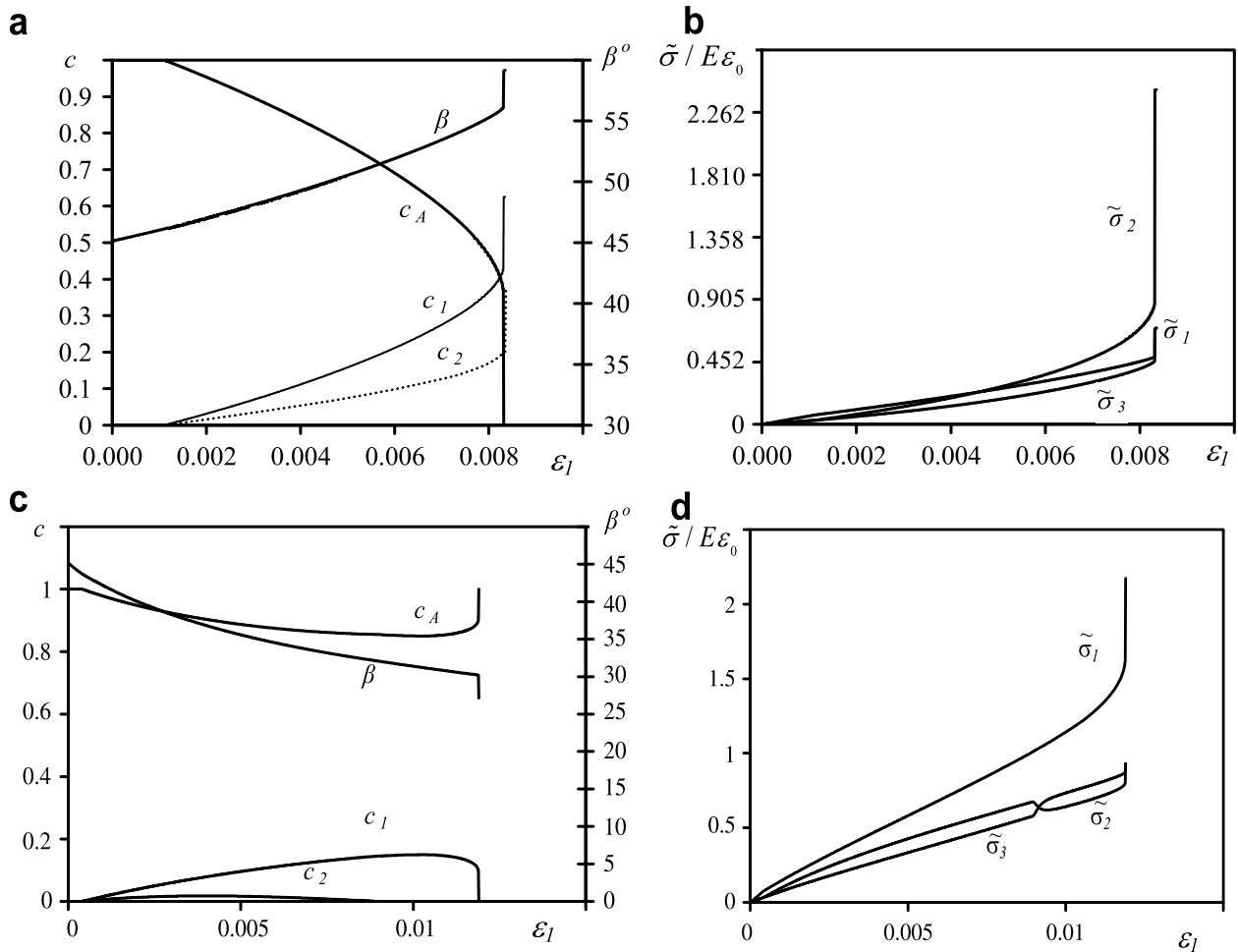


Fig. 21. For the loading $\varepsilon_2 = \varepsilon_3 = 0$ and tensile ε_1 , (a) variation of the volume fractions c_A , c_I , c_{II} and orientations β and (b) macroscopic stresses for $E_M/E_A = 4$; (c) and (d) are the same but for $E_A/E_M = 3$.

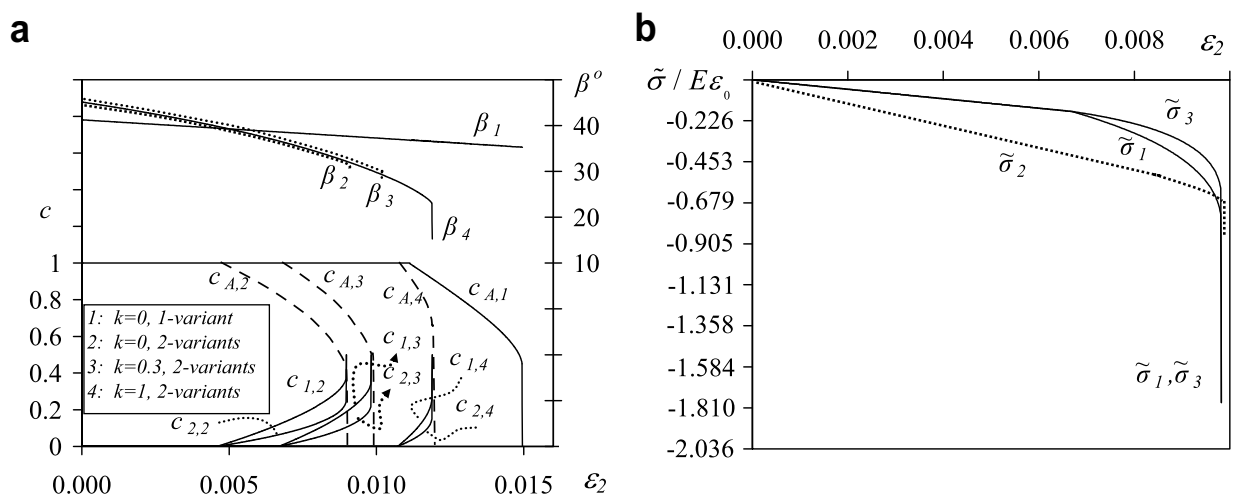


Fig. 22. For the loading $\varepsilon_1 = \varepsilon_3 = 0$ and compressive ε_2 , (a) variation of volume fractions c_A , c_I , c_{II} and the orientation β and (b) variation of stresses $\tilde{\sigma}_1$, $\tilde{\sigma}_2$ and $\tilde{\sigma}_3$ for $k = 0.0014$.

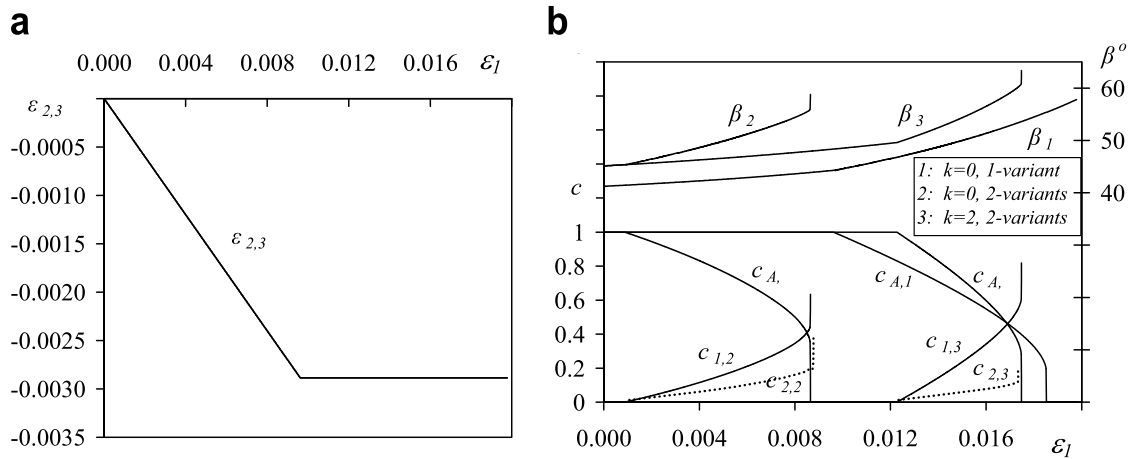


Fig. 23. (a) Loading history when only one martensitic variant is present during the phase transformation. For all cases, $\varepsilon_2 = \varepsilon_3 = -v\varepsilon_1$ before the phase transformation (uniaxial stress), and $\varepsilon_2 = \varepsilon_3 = \text{constant}$ while ε_1 is increasing after the phase transformation. (b) The variations of the volume fractions c_A, c_I, c_{II} and the change in orientations β_i .

varies from $\beta = 45.1^\circ$ to $\beta = 27.8^\circ$ inside the embryo and to $\beta = 15.3^\circ$ when $\tilde{k} = 0.091$. There is not any stress relaxation due to phase transformation. Stresses jump along with jumps in volume fraction.

4. In Fig. 23, the uniaxial stress ($\varepsilon_2 = \varepsilon_3 = -v\varepsilon_1$) is applied for all cases before the transformation, then $\varepsilon_2 = \varepsilon_3 = \text{constant}$ while compression strain ε_1 is increasing during the transformation. For a single variant, the minimum of energy is independent of n_2 and n_3 . The energy is minimum for $n_3 = 0$ when two martensitic variants are involved in the transformation. The change in the orientation of the interface is almost the same for all cases after the transformation begins and it is about 14° . When two variants present, there is an orientational instability with a jump in volume fractions.
5. In Fig. 24, the straining for uniaxial stress $\tilde{\sigma}_1$ with $\tilde{\sigma}_2 = \tilde{\sigma}_3 = 0$ is shown for different values of the athermal threshold \tilde{k} for the two variant case. The second variant first appears in a small amount and then disappears before completing the transformation. The change in orientation decreases after the second variant disappears in all cases. Inside the embryo, the curves partially overlap and transformation starts at larger values of β as \tilde{k} gets larger. The change in β is about 7° for all cases. The non-linearity in the stress–strain curve when the second variant disappears is due to a change in the interface reorientation.
6. The loading in Fig. 25 is $\varepsilon_2 = \varepsilon_3 = -0.3\varepsilon_1$ for various \tilde{k} , $\Delta\tilde{\psi} = 0.0091$ with optimal and non-optimal orientation β in an embryo. One can observe the results with both discontinuous and large continuous interface rotation after the beginning of the transformation. Curve β_1 represents the change in interface orientation when the normal is optimal in the embryo and $\tilde{k} = 0$. All other β 's correspond to the non-optimal normal $\mathbf{n} = (0.7746, 0.6325, 0)$ inside the embryo. When $\tilde{k} = 0$ for non-optimal normal orientation in the embryo, the orientation jumps to the optimal one with a small jump in volume fraction when phase transformation starts. When $\tilde{k} = 0.0045$, as soon as phase transformation starts, a jump in the orientation occurs at the same point as

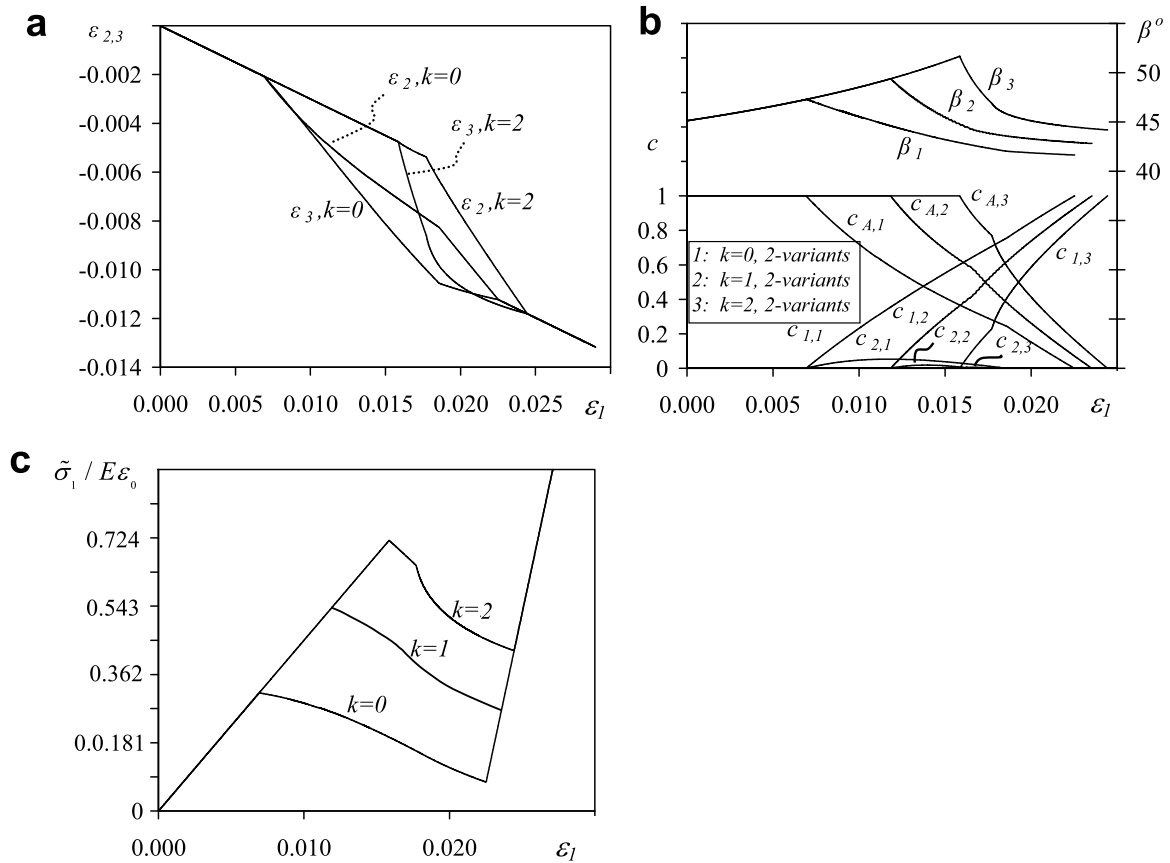


Fig. 24. (a) Straining for uniaxial loading (the case with $k = 1$ MPa is not shown), (b) the variation of volume fractions c_A, c_I, c_{II} and change in orientations β for different values of k (MPa) when the phase transformation proceeds with two variants and (c) uniaxial stresses $\tilde{\sigma}_1$ for different k values.

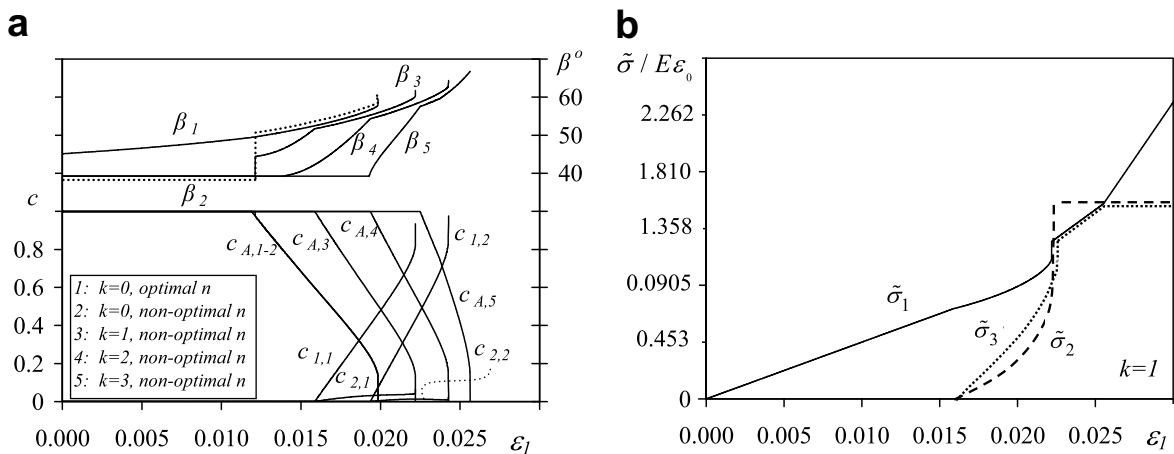


Fig. 25. (a) Variation in orientations and volume fractions c_A for the loading path $\varepsilon_2 = \varepsilon_3 = -0.3\varepsilon_1$ for various \tilde{k} with optimal and non-optimal n_0 in embryo and (b) variation in stresses $\tilde{\sigma}_1, \tilde{\sigma}_2$ and $\tilde{\sigma}_3$ for $\tilde{k} = 0.0045$.

for $\tilde{k} = 0$, but this jump is two times smaller. Then the transformation proceeds with interface rotation and without interface propagation until $X_c > 0$. For larger \tilde{k} , jumps in orientation do not occur but there is continuous interface rotation without inter-

face propagation. The volume fraction of the second variant c_2 is very small for $\tilde{k} = 0.0091$ and $\tilde{k} = 0.0136$. The orientation varies from $\beta_5 = 39.2^\circ$ to $\beta_5 = 66.8^\circ$ for $\tilde{k} = 0.0136$.

For the same loading path, variations in orientations β_i and volume fractions c_A for $\tilde{k} = 0.0136$ are shown in Fig. 26. This example is very similar to the example for tetragonal to orthorhombic transformation.

- In Fig. 27, the variation of volume fraction c_A and interface orientation β versus change in temperature ($\Delta\tilde{\psi}^\theta$) are shown for a sample in a rigid box ($\varepsilon_2 = \varepsilon_3 = \varepsilon_1 = 0$) and $\tilde{k} = 0.0001$ for an embryo of non-optimal orientation. In Fig. 27a, there is only one martensitic variant and in Fig. 27b there are two variants. Subscript “st” denotes the quasi-static change in temperature (stationary solution). For slow heating, the stationary problem is solved for each temperature. For fast heating, $\Delta\tilde{\psi}^\theta$ was given as $\Delta\tilde{\psi}^\theta = (2 - 0.000075t)/221$ where t is time in s, and non-stationary kinetics was used. For all cases, a jump in the orientation occurs from $\beta = 26.6^\circ$ to $\beta = 41.3^\circ$ as soon as

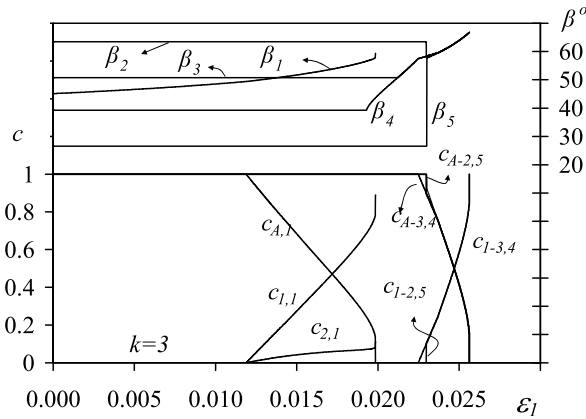


Fig. 26. Variation in orientations β_i and volume fractions c_A , c_1 , c_2 for the loading path $\varepsilon_2 = \varepsilon_3 = -0.3\varepsilon_1$ for $\tilde{k} = 0.0136$.

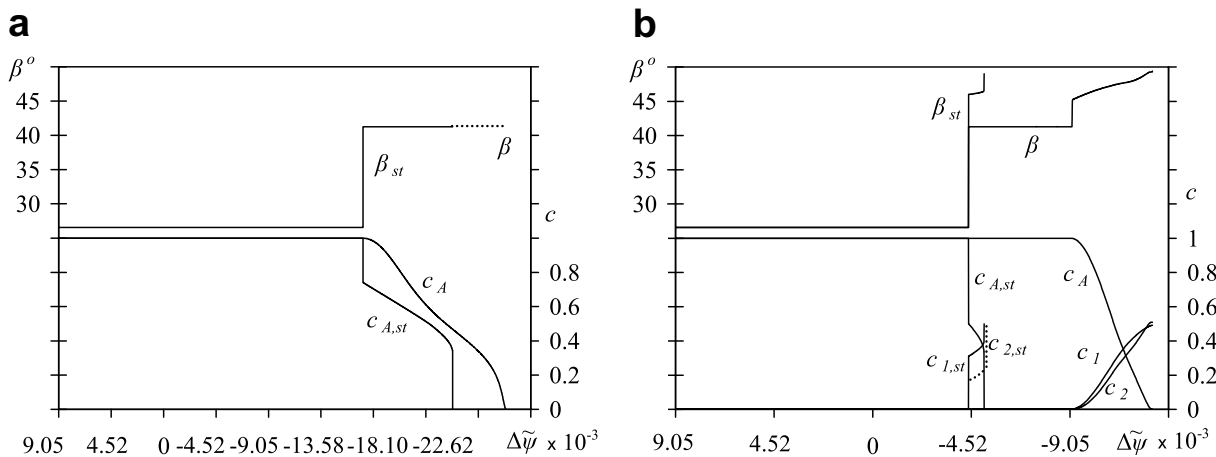


Fig. 27. Variation in volume fraction c_A and interface orientation β with the change in temperature ($\Delta\tilde{\psi}^\theta$) and $\tilde{k} = 0.0001$ for “non-optimal” embryo for (a) one-variant case and (b) for two martensitic variants. Subscript “st” denotes stationary solution for the slow change in temperature.

the phase transformation criterion is fulfilled. If the change in temperature is very slow, then the volume fractions also possess finite jumps. When the temperature change is fast and there are two variants of martensite, the normal first jumps to the value which corresponds to the optimum normal for one variant ($\beta = 41.3^\circ$) and remains the same along with very small change in volume fractions. Then, a second jump in the orientation occurs as soon as the change in volume fractions intensifies and it changes continuously until the end of phase transformation.

8. In Fig. 28, there is simultaneous change in temperature ($\Delta\tilde{\psi}^\theta$) and the loading which is $\varepsilon_2 = \varepsilon_3 = -\varepsilon_1$ versus ε_1 for $\tilde{k} = 0.0045$. Temperature and consequently $\Delta\tilde{\psi}^\theta$ is increased after transformation starts to suppress the transformation which results in a larger interface rotation. A change of 40° in the orientation during phase transformation is attainable with the proper temperature change as shown.
9. For the loading path $\varepsilon_2 = \varepsilon_3 = -0.6\varepsilon_1$ in Fig. 29 with $\tilde{k} = 0.0136$, and $\Delta\tilde{\psi}^\theta$ varied linearly from 0.0091 to 0.0231 after the phase transformation starts. Only one variant of martensite is assumed to be appearing in the calculations. The angle β varies from 41.1° to 36.2° in the embryo and then to 5° during the complete transformation that occurs for $0.0174 < \varepsilon_1 < 0.0260$.
10. For the loading given in Fig. 30a with $\tilde{k} = 0.0136$, the stresses $\tilde{\sigma}_1$, $\tilde{\sigma}_2$ and $\tilde{\sigma}_3$, change in volume fraction c_A and orientation β are shown in Fig. 30b and c. First, the material is loaded to point A where $t = 5250$ s. Then, the strains are prescribed in such a way that the averaged stresses are reduced to zero (point B). Finally, the temperature is increased to obtain austenite in the entire volume. The change in the orientation inside the embryo is from $\beta = 41.2^\circ$ to $\beta = 53.8^\circ$. After transformation starts, β continues to increase and becomes $\beta = 66.0^\circ$ at point A. During unloading which is between points A and B, there is no reverse transformation (the pseudoplastic behavior) and interface rotation, so the orientation angle stays at $\beta = 66.0^\circ$. During reverse transformation due to heating (the shape memory effect), the angle β reduces to 41.2° at the end of the complete transformation.

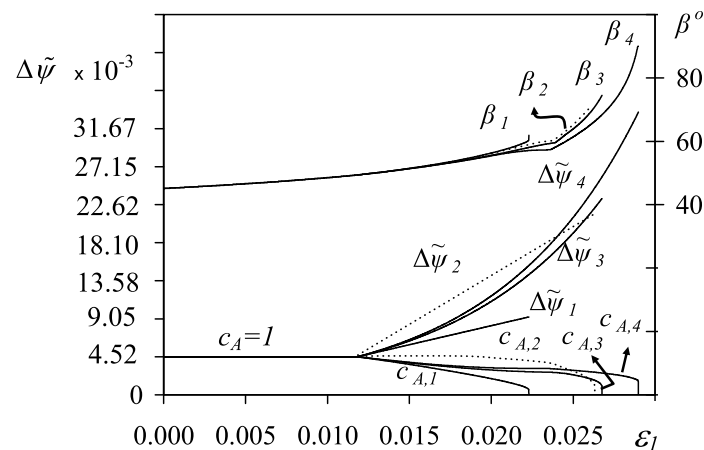


Fig. 28. Change in volume fractions c_A , orientation β and the temperature for the loading $\varepsilon_2 = \varepsilon_3 = -\varepsilon_1$ with $\tilde{k} = 0.0045$.

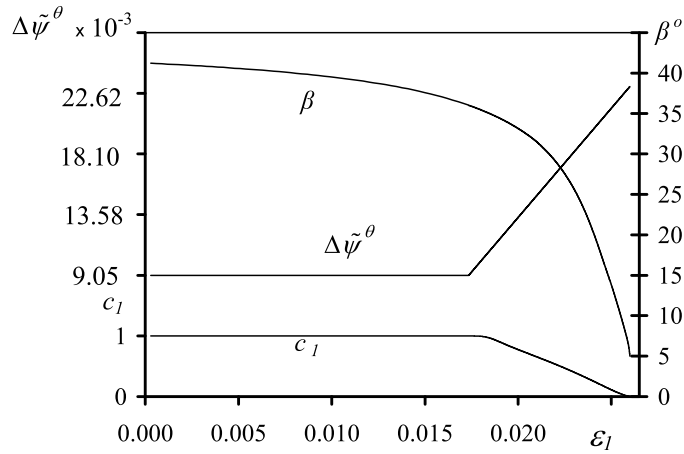


Fig. 29. For the loading path $\varepsilon_2 = \varepsilon_3 = -0.6\varepsilon_1$, $\tilde{k} = 0.0136$ and for optimal embryo with single martensitic variant, variation in volume fraction c_1 and interface orientation β with the change in temperature ($\Delta\tilde{\psi}^\theta$).

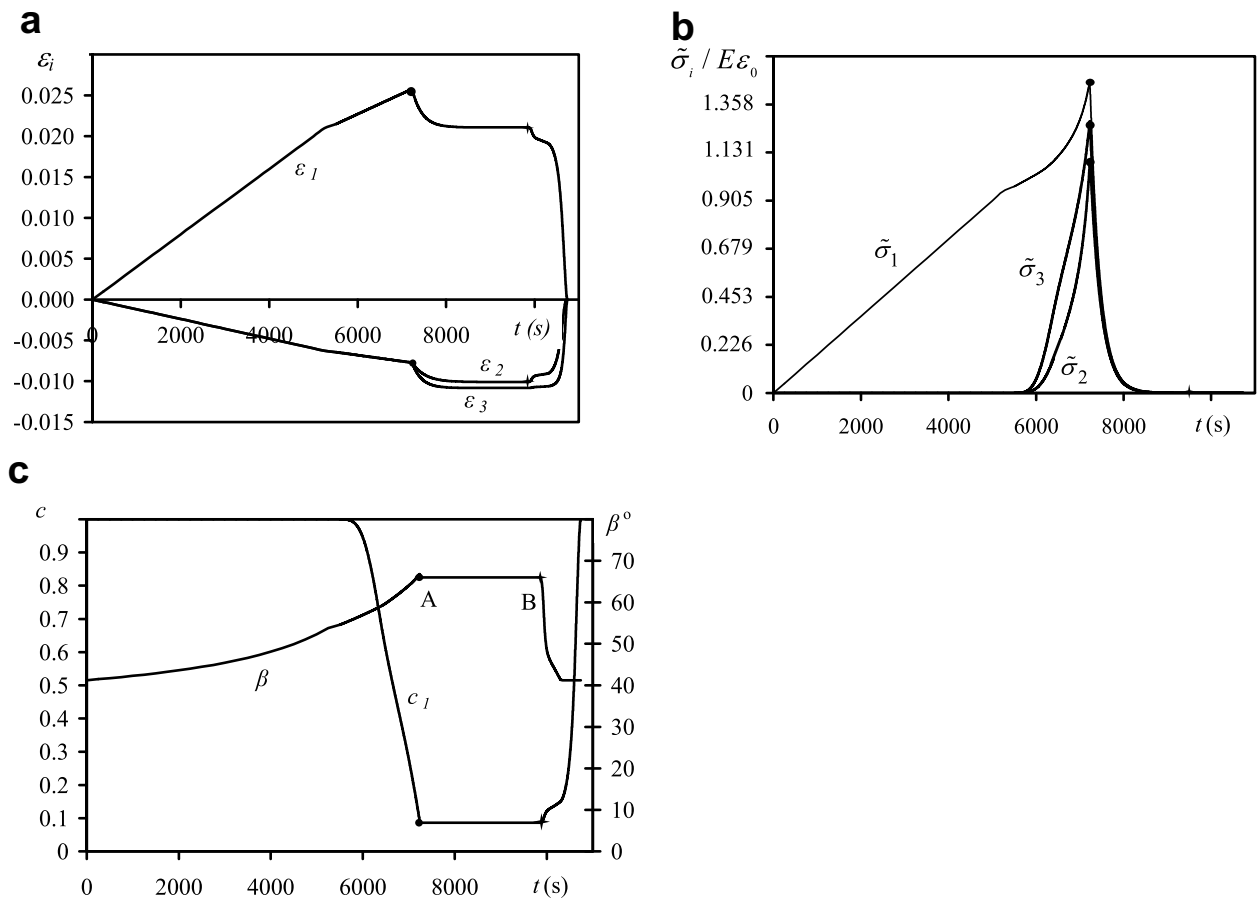


Fig. 30. (a) The loading path, (b) the change in stresses $\tilde{\sigma}_1$, $\tilde{\sigma}_2$ and $\tilde{\sigma}_3$ and (c) the variations in volume fraction c_1 and orientation β .

- For the case $E_A/E_M = 3$ and the compressive straining ε_2 with $\varepsilon_3 = -v\varepsilon_2$ and $\varepsilon_1 = 0$, the variations of the volume fractions c_A , c_I and c_{II} , and the variation in the angle β are shown in Fig. 31 for $\tilde{k} = 0.0023$ and $\tilde{k} = 0.0045$. The variation in the volume fractions of c_I and c_{II} is shown for $k = 0.0045$ only to avoid overlapping the curves.

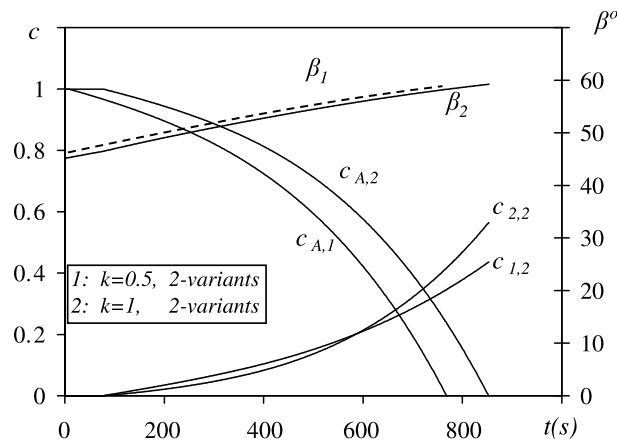


Fig. 31. The variations of the volume fractions c_A , c_I and c_{II} , and the variation in the angle β for the compressive straining ε_2 with $\varepsilon_3 = -\nu\varepsilon_2$ and $\varepsilon_1 = 0$ for $E_A/E_M = 3$.

For both examples, the change in normal follows the same curve. The only difference is that when $k = 0.0045$, the transformation is completed later. There is about 13° change in the angle β during the transformation.

To summarize, in this section we studied various simple and complex mechanical and thermomechanical loadings for cubic to tetragonal and tetragonal to orthorhombic transformations. We studied the effects of the magnitude of the athermal threshold \tilde{k} , the number of martensitic variants (one or two), as well as optimal and non-optimal normal in the embryo. Depending on the loading process, the effect of these parameters is very different. We observed large continuous change in interface orientation, jump in interface reorientation (behavior energetically similar to the first-order phase transformation), jump in volume fractions and stresses, expected stress relaxation during the phase transition and unexpected stress growth during the transition because an increase in elastic strain due to an increase in elastic moduli (for direct or reverse transformation) exceeds their decrease due to the transformation strain. Our examples provide important information on how to design the loading process to obtain various strong effects related to interface reorientation that can be checked experimentally.

8. Concluding remarks

In Part 2 of the paper, we formulated a complete system of equations that describes evolution of stresses in phases and crystallographic parameters, as well as macroscopic stress–strain response for martensitic phase transformations under complex multiaxial loadings. Algorithms for the solution of this system are presented. First, we studied the case without interface rotation. The effect of the athermal thresholds for A–M and M_I – M_{II} interfaces and loading paths on stress–strain curves and phase transformations was studied. We found that the deviation of the stress–strain curve from the curve with zero dissipation is non-symmetric and that the behavior inside the hysteresis loop is very complex. Both of these results are related to activation and suppressing the variant–variant transformation depending on the loading path and athermal thresholds. The macroscopic

stress decreases during the direct phase transformation under loading and increases during the reverse transformation under unloading. This behavior is caused by internal stresses due to incompatible transformation strain. These properties lead to material instability in the solution of a boundary-value problem for a finite sample which have to result in localization of transformation strain and formation of the discrete martensitic microstructure (see Levitas et al., 2004; Idesman et al., 2005). Thus, these micromechanically-based constitutive equations can be used in finite element simulation of the discrete multiconnected martensitic microstructure instead of pure phenomenological models in Levitas et al. (2004) and Idesman et al. (2005). These properties, however, complicate direct comparison of our results with experimentally obtained stress–strain curves, because for unstable behavior, the local and macroscopic stress–strain curves differ significantly.

Second, we presented various non-trivial examples of combined interface propagation and interface rotation under complex loading. We varied the magnitude of the athermal threshold \tilde{k} , the number of martensitic variants (one or two), as well as studied the effect of the interface orientation in the embryo. We found that an instability in the interface normal leads to a jump-like interface reorientation that has the following features of the energetics of a first-order transformation: there are multiple energy minima in the space of components of the interface normal \mathbf{n} that are separated by an energy barrier; positions of minima do not change during loading but their depth and barriers vary; when the barrier disappears (i.e. one of the minima transforms to the local saddle or maximum points), the system rapidly evolves toward another stable orientation. The jump in the interface orientation is accompanied by jumps in volume fractions and stresses. We also observed large continuous change in interface orientation and expected stress relaxation during the phase transition. However, in some cases, an unexpected stress growth during the transition is observed, because the increase in elastic strain due to an increase in elastic moduli (for direct or reverse transformation) exceeds their decrease due to transformation strain. Our examples provide important information on how to design the loading process to obtain various strong effects related to interface reorientation that can be checked experimentally and that will hopefully motivate related experimental studies. Since points of a single, and especially polycrystalline sample, are subjected to complex loading, even for uniaxial macroscopic loading (Levitas et al., 2004; Idesman et al., 2005), the interface reorientation plays an important role in microstructure evolution. Our results can also motivate improvement of less detailed models, presented, e.g., in Sun and Hwang (1993), Marketz and Fischer (1996), Levitas and Stein (1997), Liu and Xie (2003), Thamburaja (2005), Pan et al. (2007), Popov and Lagoudas (2007), Auricchio et al. (2007), Hall et al. (2007), Shaw (2000), Muller and Bruhns (2006), Stupkiewicz and Petryk (2002) and Gao et al. (2000).

A similar approach can be applied for finite strains, based on the theory in (Levitas and Ozsoy, 2008). The next step will be related to a generalization that accounts for plastic accommodation by slip. This is a very sophisticated problem and its solution will be based on the general theory of phase transformations in elastoplastic materials developed in (Levitas, 1998, 2000).

Acknowledgements

NSF (CMS-0555909), LANL, and TTU support as well as collaboration with Dean Preston (LANL) are gratefully acknowledged.

References

- Auricchio, F., Reali, A., Stefanelli, U., 2007. A three-dimensional model describing stress-induced solid phase transformation with permanent inelasticity. *Int. J. Plasticity* 23 (2), 207–226.
- Bhattacharya, K., 2004. *Microstructure of Martensite. Why It Forms and How It Gives Rise to the Shape-memory Effect*. Oxford University Press, New York.
- Gao, X., Huang, M., Brinson, L.C., 2000. A multivariant micromechanical model for SMAs. Part 1. Crystallographic issues for single crystal model. *Int. J. Plasticity* 16 (10), 1345–1369.
- Hall, G.J., Govindjee, S., Sittner, P., Novak, V., 2007. Simulation of cubic to monoclinic-II transformations in a single crystal Cu–Al–Ni tube. *Int. J. Plasticity* 23 (1), 161–182.
- Idesman, A.V., Levitas, V.I., Preston, D.L., Cho, J.-Y., 2005. Finite element simulations of martensitic phase transitions and microstructure based on strain softening model. *J. Mech. Phys. Solids* 53 (3), 495–523.
- Levitas, V.I., Stein, E., 1997. Simple micromechanical model of thermoelastic martensitic transformations. *Mech. Res. Commun.* 24, 309–318.
- Levitas, V.I., 1998. Thermomechanical theory of martensitic phase transformations in inelastic materials. *Int. J. Solids Struct.* 35, 889–940.
- Levitas, V.I., 2000. Structural changes without stable intermediate state in inelastic material. Part I and II. *Int. J. Plasticity* 16 (7–8), 805–849, 851–892.
- Levitas, V.I., Idesman, A.V., Preston, D., 2004. Microscale simulation of evolution of martensitic microstructure. *Phys. Rev. Lett.* 93 (10), 105701-1.
- Levitas, V.I., Ozsoy, I.B., Preston, D.L., 2007. Interface reorientation during coherent phase transformations. *Europhys. Lett.* 78, 16003.
- Levitas, V.I., Ozsoy, I.B., 2008. Micromechanical modeling of stress-induced phase transformations. Part I. Thermodynamics and kinetics of coupled interface propagation and reorientation. *Int. J. Plasticity*. doi:10.1016/j.ijplas.2008.02.004.
- Liu, Y., Xie, Z.L., 2003. Twinning and detwinning of $\langle 011 \rangle$ type II twin in shape memory alloy. *Acta Mater.* 51 (18), 5529–5543.
- Marketz, F., Fischer, F.D., 1996. Modelling the mechanical behavior of shape memory alloys under variant coalescence. *Comput. Mater. Sci.* 5 (1-3), 210–226.
- Muller, C., Bruhns, O.T., 2006. A thermodynamic finite-strain model for pseudoelastic shape memory alloys. *Int. J. Plasticity* 22 (9), 1658–1682.
- Pan, H., Thamburaja, P., Chau, F.S., 2007. Multi-axial behavior of shape-memory alloys undergoing martensitic reorientation and detwinning. *Int. J. Plasticity* 23 (4), 711–732.
- Pankova, M.N., Roytburd, A.L., 1984. Orienting influence of applied stress on the martensitic transformation in alloys based on iron. *Phys. Met. Metall.* 58 (4), 81–90.
- Popov, P., Lagoudas, D.C., 2007. 3-D constitutive model for shape memory alloys incorporating pseudoelasticity and detwinning of self-accommodated martensite. *Int. J. Plasticity* 23 (10–11), 1679–1720.
- Roytburd, A.L., Kosenko, N.S., 1976. Orientational dependence of the elastic energy of a plane interlayer in a system of coherent phases. *Phys. Stat. Sol. A* 35 (2), 735–746.
- Roytburd, A.L., Slutsker, J., 2001. Deformation of adaptive materials. Part III: Deformation of crystals with polytwin product phases. *J. Mech. Phys. Solids* 49 (8), 1795–1822.
- Shaw, J.A., 2000. Simulation of localized thermo-mechanical behaviour in a NiTi shape memory alloy. *Int. J. Plasticity* 16 (5), 541–562.
- Stupkiewicz, S., Petryk, H., 2002. Modelling of laminated microstructures in stress-induced martensitic transformations. *J. Mech. Phys. Solids* 50 (11), 2303–2331.
- Sun, Q.P., Hwang, K.C., 1993. Micromechanics modelling for the constitutive behavior of polycrystalline shape memory alloys. I. Derivation of general relations. *J. Mech. Phys. Solids* 41 (1), 1–17.
- Thamburaja, P., 2005. Constitutive equations for martensitic reorientation and detwinning in shape-memory alloys. *J. Mech. Phys. Solids* 53 (4), 825–856.